CO_2 conversion in a gliding arc plasma : 1D cylindrical discharge model

CO$_2$ conversion in a gliding arc plasma: 1D cylindrical discharge model

Weizong Wang[1], **Antonin Berthelot**[1], **Stanimir Kolev**[2], **Xin Tu**[3] and **Annemie Bogaerts**[1]

[1] Research group PLASMANT, Department of Chemistry, University of Antwerp, Universiteitsplein 1, B-2610 Wilrijk-Antwerp, Belgium
[2] Faculty of Physics, Sofia University, 5 James Bourchier Boulevard, 1164 Sofia, Bulgaria
[3] Department of Electrical Engineering and Electronics, University of Liverpool, Brownlow Hill, Liverpool L69 3GJ, UK

E-mail: wangweizong@gmail.com and annemie.bogaerts@uantwerpen.be

Abstract

CO$_2$ conversion by a gliding arc plasma is gaining increasing interest, but the underlying mechanisms for an energy-efficient process are still far from understood. Indeed, the chemical complexity of the non-equilibrium plasma poses a challenge for plasma modeling due to the huge computational load. In this paper, a one-dimensional (1D) gliding arc model is developed in a cylindrical frame, with a detailed non-equilibrium CO$_2$ plasma chemistry set, including the CO$_2$ vibrational kinetics up to the dissociation limit. The model solves a set of time-dependent continuity equations based on the chemical reactions, as well as the electron energy balance equation, and it assumes quasi-neutrality in the plasma. The loss of plasma species and heat due to convection by the transverse gas flow is accounted for by using a characteristic frequency of convective cooling, which depends on the gliding arc radius, the relative velocity of the gas flow with respect to the arc and on the arc elongation rate. The calculated values for plasma density and plasma temperature within this work are comparable with experimental data on gliding arc plasma reactors in the literature. Our calculation results indicate that excitation to the vibrational levels promotes efficient dissociation in the gliding arc, and this is consistent with experimental investigations of the gliding arc based CO$_2$ conversion in the literature. Additionally, the dissociation of CO$_2$ through collisions with O atoms has the largest contribution to CO$_2$ splitting under the conditions studied. In addition to the above results, we also demonstrate that lumping the CO$_2$ vibrational states can bring a significant reduction of the computational load. The latter opens up the way for 2D or 3D models with an accurate description of the CO$_2$ vibrational kinetics.

Keywords: CO$_2$ conversion, gliding arc, non-equilibrium plasma, vibrational levels, level-lumping, plasma chemistry, splitting mechanisms

(Some figures may appear in colour only in the online journal)

1. Introduction

The conversion of CO$_2$ and CH$_4$ into value-added chemicals and liquid fuels is gaining increasing interest due to the rising greenhouse gas concentration in the atmosphere, which has a great impact on global weather pattern. Conventional methods of CH$_4$ and CO$_2$ conversion require quite a large amount of energy, and this has led to a major interest in alternative reforming techniques in pursuit of milder reaction conditions with reduced energy costs. In this respect, atmospheric plasmas offer unique perspectives because of their capacity to induce chemical reactions within gases with a limited energy cost at ambient pressure and temperature. One of the most effective and promising plasmas for this application is a gliding arc, commonly known as a GlidArc [1–4]. A gliding arc is a non-stationary discharge, usually operating

at atmospheric pressure and generating a non-equilibrium plasma. It is gaining interest for high efficiency chemical applications, because it can produce a large density of highly reactive species.

In the last 10 years, there is a growing interest for GlidArc applications in gas conversion, such as CH_4 partial oxidation [5, 6], CO_2 reforming of CH_4, also called dry reforming of methane (DRM), to produce syngas ($CO + H_2$) [7, 8], and CO_2 splitting [9–11]. For DRM, the maximum conversions reported in literature are around 5–15%, depending on the conditions, with energy efficiencies up to 60% [7]. For CO_2 splitting, conversions up to 18% have been reached, with energy efficiencies up to 43% [9].

In order to improve these applications, the physical and chemical characteristics of the GlidArc have been extensively studied by experiments, including electrical measurements [7, 12], spectroscopic measurements [13, 14], and high-speed photography [15]. Besides these experiments, detailed modelling is very useful to obtain a better insight in the underlying processes and to optimize the plasma conditions. However, only a few papers in the literature deal with GlidArc modelling, typically applying a 1D analytical model, such as the Elenbaas–Heller model [2], or the plasma string model [16, 17], assuming equilibrium conditions and a constant radius of the plasma channel, or with a correction based on an analytical relation between the electric field and the electron and gas temperature for non-equilibrium plasma [18]. A detailed description of the chemical reactions occurring in the gliding arc, which will determine the gas conversion, was however ignored in the above models. In order to fully describe the discharge properties of a gliding arc, more extensive simulations with detailed plasma kinetics are greatly needed.

Recently, a comprehensive 2D non-quasi-neutral model of an argon gliding arc, considering the interactions between the arc plasma column and the electrodes, as well as detailed plasma kinetics, was presented by Kolev and Bogaerts, to study the arc root movement [19]. In a follow-up paper [20], a comparative study of gliding glow and gliding arc discharges was performed to describe the different mechanisms of the plasma channel attachment to the cathode, which can lead to different plasma properties. Moreover, a 3D quasi-neutral model for a reverse vortex flow gliding arc in argon was also recently reported [21]. However, to our knowledge, no models exist yet for a gliding arc used for greenhouse gas conversion, like CO_2 splitting. Indeed, the latter is really challenging, due to the chemical complexity of this non-equilibrium plasma. Not only do many species have to be taken into account, but also the internal states, like the vibrationally excited levels, have to be dealt with, because of the non-equilibrium characteristics of the plasma. Indeed, the excitation of the asymmetric vibrational mode of CO_2 appears to be a very efficient way to enhance the dissociation, yielding a high energy efficiency in warm plasmas, as was already demonstrated for microwave discharges [22]. The same can be true for a gliding arc plasma, which is also considered as a warm plasma [23].

To describe the different conversion mechanisms taking place in such a discharge, including vibration-induced dissociation of CO_2, a large number of processes among the

vibrational levels, such as vibrational–vibrational (VV) and vibrational–translational (VT) relaxation, need to be taken into account [24, 25]. The large number of species and related chemical reactions makes spatially resolved models computationally expensive. That is why most of the numerical studies undertaken so far on the subject have been limited to 0D models [24–30]. In order to model a CO_2 plasma in more dimensions, the chemistry set needs to be considerably reduced, without the loss of essential information. Recently, our group reduced the complexity and the number of species included in the chemistry set from the previous work [24, 25] and developed a reduced chemistry set for a CO_2 microwave plasma, among others by lumping the vibrational levels [31]. By means of a 0D model of a microwave plasma, it was illustrated that the level-lumping method can reproduce the vibrational distribution function (VDF) very well and this will enable 2D or 3D modeling of CO_2 conversion in a microwave discharge.

In the present paper, for the first time, we present a 1D quasi-gliding arc model for CO_2, with a detailed non-equilibrium CO_2 plasma chemistry set, including a description of the vibrational kinetics up to the dissociation limit. The term 'quasi-gliding' refers to the fact that the real arc movement due to the convective gas flow is not taken into account here as a result of the limited dimensionality of the model. However, the influence of convective gas flow on the discharge properties is accounted for by using a characteristic frequency of convective cooling, which depends on the gliding arc radius, the relative velocity of the gas flow with respect to the arc and the arc elongation rate. Therefore, we believe this model resembles the characteristics of a real gliding arc.

The fact that we take into account the detailed plasma chemistry under both thermal and chemical non-equilibrium is a distinct improvement compared to previous 1D gliding arc models [2, 16, 17]. Thus, this paper provides important details about the reaction kinetics for CO_2 splitting in a gliding arc. Moreover, we will assess the effectiveness of the vibrational states lumping method for the gliding arc, as the latter can yield a great reduction of the computational load when aiming to model a gliding arc for CO_2 conversion in 2D or 3D at a later stage.

The paper is organized as follows. In section 2, we describe the self-consistent 1D model, and we present the chemistry set, including the considered species and reactions, as well as the level-lumping strategy. In section 3, we show the calculation results for typical discharge currents and characteristic frequencies of convective plasma cooling with a laminar gas flow, under both quasi-steady state and transient conditions, corresponding to a DC and AC gliding arc, respectively. Our calculated values for plasma density and plasma temperature, as well as the time evolution of the electric field, are qualitatively compared with experimental results for gliding arc reactors in literature. We also investigate the dominant splitting mechanisms of CO_2 in the gliding arc, and we will refer to experimental evidence from literature. Moreover, the influence of the gas flow rate on the power efficiency of CO_2 conversion is presented by comparing our predicted results under different characteristic frequencies of convective plasma
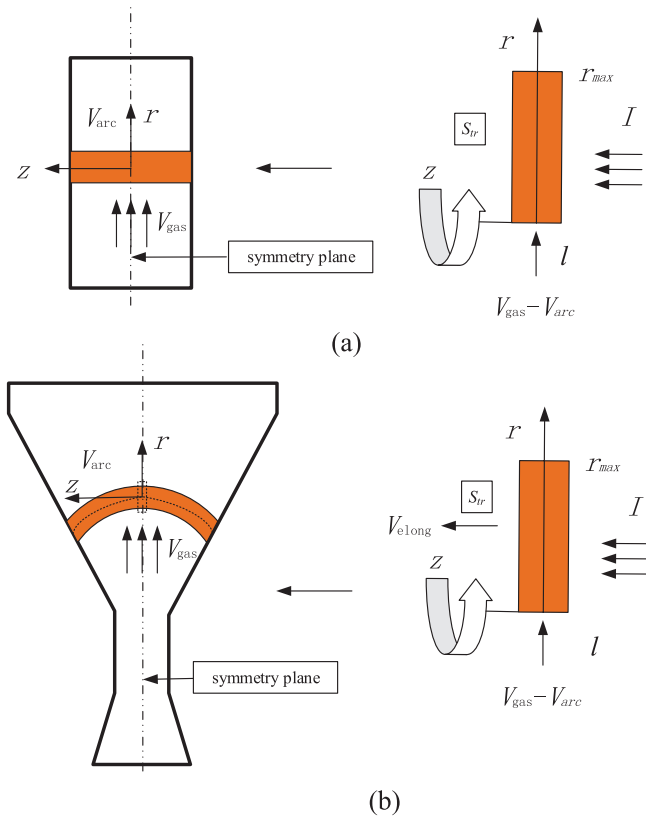
Figure 1. Schematic illustration of the gliding arc geometry, with indication of the quasi-cylindrical arc (left) and the 1D simulation region (right) for the parallel plate gliding arc reactor (a) and diverging electrodes gliding arc reactor (b).

cooling with experimental work. In addition, we compare the results of the level lumping method, for different numbers of grouped levels, with the results obtained by the full model treating all individual excited levels. Finally, a conclusion will be given in section 4.

2. Description of the model

2.1. Geometry and treatment of convective cooling in the model

There exist two types of (classical) gliding arc reactors with different velocity distributions [18]. For a parallel plate gliding arc reactor with fixed gap separation, the gas velocity is the same at every point in the reactor. On the other hand, for a so-called diverging electrodes gliding arc reactor, where the gap separation between both electrodes changes as a function of height, the velocity of the gas decreases with increasing gap separation, and thus increases the length of the arc. Figure 1 shows a schematic picture of both the parallel plate gliding arc reactor (a) and the diverging electrodes gliding arc reactor (b), with indication of the simulation region in the 1D model, where only the radial direction of the quasi-cylindrical arc discharge channel is taken into account. In this model, we consider a transverse cross section of the plasma string along the symmetry plane of the reactor, excluding the longitudinal coordinate along the

discharge current, as indicated by the small dashed box in figure 1 (left part). The gliding arc is then simply described as a conducting channel in an axi-symmetrical cylindrical geometry (see figure 1, right part). A similar treatment was applied in 1D analytical models of a gliding arc in literature, such as the Elenbaas–Heller model [2] and the plasma string model [16, 17]. A distinct improvement compared to the previous gliding arc models is, however, that we take into account the detailed plasma chemistry of CO_2 under both thermal and chemical non-equilibrium, as described in the next section. Additionally, we take into account the loss of plasma species and heat due to convection in the arc, by introducing an effective convective frequency of the gas in the arc (see details below), which allows our model to better represent the specific properties of the gliding arc.

Indeed, in reality the discharge channel of the gliding arc is shifted downstream by the gas flow (see figure 1, V_{gas}). Hence, the discharge channel does not have a standard axi-symmetrical cylindrical geometry, and thus in principle a 2D or 3D description of the gliding arc dynamics would be more adequate. However, an investigation of the discharge contraction under influence of a gas flow by means of a cylindrical model with axial symmetry showed agreement with the results of a plane model and with experiments [32, 33], indicating that such a treatment may describe the qualitative behaviour of the discharge and provide valuable results. Therefore, we have adopted the same approach.

Several experimental studies (e.g. [2, 17]) have shown that there exists a lag of the gliding arc with respect to the gas flow. The ratio of their velocities (V_{gas}/V_{arc} in figure 1) is usually 1.1–1.7 and is very dependent on the gas flow velocity, the applied power and even the arc length [17]. Usually the difference is larger for higher gas flow velocities and it decreases with increasing arc length [17]. It is clear that the relative velocity of the gas flow with respect to the arc, $V_{rel} = V_{gas} - V_{arc}$, considerably affects the discharge behaviour. More specifically, the cooling efficiency of the gliding arc conductive channel increases with the increasing relative velocity and this indicates the important effect of the forced convection on the physical properties of the gliding arc. The mechanism causing the gliding arc lag is quite complicated, and is beyond the scope of our current work, because of the 1D model. However, we take into account the influence of the relative velocity of the gas flow with respect to the arc by introducing a characteristic frequency of convective cooling, which is described in detail below.

If we take the gliding arc as the frame of reference, the gas convection effect as a result of the relative velocity of the gas flow with respect to the gliding arc is taken into account as a simple dilution of the arc by the incoming background gas, which blasts the species densities and energy out of the discharge channel. For an elementary domain with a characteristic length l in the direction of the discharge current and a discharge channel radius r_{max}, the volume of the background gas flowing into the discharge channel (circular cross section) will increase with $d\Omega = lV_{rel}(2r_{max})dt$ within a time period dt, due to the relative velocity $V_{rel} = V_{gas} - V_{arc}$. It is noted that the value of $d\Omega$ in the limit of infinitesimal displacement

for a circular cross section in this work is identical with that for a square cross section with a width of $2r_{max}$ because both the semicircle and the side of rectangle have the same projection length in the direction perpendicular to the gas flow. Correspondingly, the volume of plasma flowing out of the discharge channel will also increase by $d\Omega$. Due to the laws of conservation, a variable φ will be reduced by $d\varphi$, which is defined as the difference between the initial value φ and the value after the dilution φ_{dilu} by the relative velocity. Because the variables are conserved $\varphi(\Omega - d\Omega) + \varphi_{bg}d\Omega = \varphi_{dilu}\Omega$, we can determine $d\varphi$ as follows

$$
\begin{aligned}
d\varphi = \varphi - \varphi_{dilu} &= \varphi - \frac{\varphi(\Omega - d\Omega) + \varphi_{bg}d\Omega}{\Omega} \\
&= \frac{\varphi\Omega - [\varphi(\Omega - d\Omega) + \varphi_{bg}d\Omega]}{\Omega} \\
&= \frac{(\varphi - \varphi_{bg})d\Omega}{\Omega} \\
&= \frac{(\varphi - \varphi_{bg})l(2r_{max})V_{rel}dt}{l\pi(r_{max})^2} \\
&= \frac{(\varphi - \varphi_{bg})V_{rel}dt}{(\pi r_{max}/2)} \\
&= \frac{(\varphi - \varphi_{bg})V_c dt}{L_c}
\end{aligned}
\tag{1}
$$

where $L_c = \pi r_{max}/2$ and $V_c = V_{rel}$ are defined as the characteristic length and the characteristic velocity for the relative movement of gliding arc with regard to gas flow, respectively, and the parameter φ_{bg} is the background value of the variable φ. In the model, we take the background values of almost all variables to be calculated (i.e. the species number densities and the average electron energy density; see below) as zero, except for the gas temperature (taken as $T_g = 293$ K) and the number densities of the various excited states of CO_2, for which the background values are assumed to follow a Maxwellian distribution at $T_g = 293$ K.

Besides the plasma dilution caused by the relative velocity between gas flow and gliding arc, for the diverging electrodes gliding arc reactor, the gliding arc elongation when the arc moves downstream also contributes to the loss of species densities and energy in the discharge channel. In [20] the effect of the gas convection is taken into account as a simple stretching (elongation) of the arc, which redistributes the species and their energy over a larger volume. In that paper, a similar form of the variables reduction $d\varphi = (\varphi - \varphi_{bg})V_{elong}dt/L_{arc}$ as a result of the arc elongation is derived. Here, the characteristic velocity and length are replaced by the arc elongation velocity V_{elong} and the arc length L_{arc}.

As we discussed above, the influence of gas convection on the loss of the species densities and energy includes both the contribution from the relative velocity between gas flow and arc, and the arc elongation. Both act together and they can be considered effectively within the same approach as presented in formula (1). Thus, the effective loss term due to gas convection is given by:

$$
\begin{aligned}
\frac{d\varphi}{dt} &= \frac{(\varphi - \varphi_{bg})V_{rel}}{(\pi r_{max}/2)} + \frac{(\varphi - \varphi_{bg})V_{elong}}{L_{arc}} \\
&= \frac{\varphi - \varphi_{bg}}{\tau 1} + \frac{\varphi - \varphi_{bg}}{\tau 2} \\
&= (\varphi - \varphi_{bg})(F1 + F2) \\
&= (\varphi - \varphi_{bg})F
\end{aligned}
\tag{2}
$$

where $\tau 1 = (\pi r_{max}/2)/V_{rel}$ and $\tau_2 = L_{arc}/V_{elong}$ are the characteristic time of convective plasma cooling with a laminar gas flow due to the relative velocity and the arc elongation, respectively. We define here a characteristic frequency $F = 1/\tau$ to describe the effect of convective cooling, following a similar treatment as in [20].

Note that both the relative velocity of the gas flow with respect to the arc and the arc elongation velocity are very dependent on the gas flow velocity, the applied power and even the arc length. For example, a larger gas flow rate generally yields a higher relative velocity and arc elongation velocity, leading to an enhanced convective removal of the species densities and energy. In the experiments of [17], typical values of the relative velocity ranging from zero to 28 m s^{-1} are obtained for different conditions. Correspondingly, the characteristic frequency of convective cooling also changes, not only in time, but also in space. At this point, our goal is not to make an accurate simulation of a specific experimental setup, but to provide general insight into the quasi-gliding arc discharge behaviour under the effect of convective cooling. Therefore, we consider a constant value of this characteristic frequency of convective cooling, and we will perform several simulations to evaluate the effect of this parameter on the arc discharge behaviour. As discussed above, both the relative velocity between gas flow and arc, and the arc elongation, contribute to the convective removal of the species densities and energy, and can be expressed in the same way with an effective convective cooling frequency (see equation (2)). Thus, our method is valid for both a parallel plate gliding arc reactor (figure 1(a)), where the convective cooling is only due to the relative velocity between gas flow and arc, as well as for a diverging electrodes gliding arc reactor (figure 1(b)), where the convective losses are due to both the relative velocity between gas flow and arc, and the elongation of the arc.

Considering a simple cylindrical geometry (i.e. corresponding to a parallel plate reactor), in the assumed cylindrical geometry, we define $L_c = \pi r_{max}/2$, where r_{max} is the radius of the quasi-cylinder occupied by the arc plasma, for which a typical value of 2 mm is taken. The latter is based on data obtained by theoretical calculations and high speed camera experiments [16, 17]. For a characteristic length of $L = \pi$ (mm) (see above), relative velocities of 3.9 m s^{-1}, 7.9 m s^{-1} and 15.7 m s^{-1} (see above) correspond to characteristic frequencies of convective cooling of 1.25 kHz, 2.5 kHz and 5 kHz, respectively. For the diverging electrodes gliding arc reactor, it is a bit more difficult to correlate the characteristic frequencies of convective cooling with the actual conditions, because of the double effect due to (i) the relative velocity between gas flow and arc and (ii) the arc elongation. Note that a higher value of this characteristic frequency of convective

cooling means a more effective removal of the plasma variables, like the species number densities, the average electron energy density and the specific enthalpy, from the discharge channel due to convection (see equation (2)), as a result of the relative velocity of the gas flow with respect to the arc.

2.2. Equations solved in the model

The model calculates the plasma species densities, the electron and gas temperature and the electric field in the gliding

For the neutral species, the flux is only determined by diffusion:

$$\overrightarrow{G_s} = -D_s \nabla n_s \tag{8}$$

q_s is the charge of the given species type. D_s is the diffusion coefficient and μ_s is the mobility of the corresponding species. The ambipolar electric field $\overrightarrow{E_{amb}}$ is derived from the various charged species:

$$\overrightarrow{E_{amb}} = \frac{D_{CO_2^+}\nabla n_{CO_2^+} + D_{O_2^+}\nabla n_{O_2^+} - D_{CO_3^-}\nabla n_{CO_3^-} - D_{O^-}\nabla n_{O^-} - D_{O_2^-}\nabla n_{O_2^-} - D_e\nabla n_e}{n_{CO_2^+}\mu_{CO_2^+} + n_{O_2^+}\mu_{O_2^+} + n_{CO_3^-}\mu_{CO_3^-} + n_{O^-}\mu_{O^-} + n_{O_2^-}\mu_{O_2^-} + n_e\mu_e} \tag{9}$$

arc. We assume electrical neutrality in the plasma, because the sheath is not considered in our model, and this assumption has no significant influence on the arc column [34]. The following equations are solved.

The species density continuity equations read as follows:

$$\frac{\partial n_s}{\partial t} + \nabla \overrightarrow{G_s} = S_{c,s} - (n_s - (n_s)_{bg})F. \tag{3}$$

Here, n_s is the species density, and $S_{c,s}$ is the collision term representing the net number of particles produced (when a positive value) or lost (when negative) in the volume reactions. The last term in the right-hand side accounts for the loss of plasma species in the arc due to the convective flow, as explained above. The index 's' represents all the species considered in the model (see section 2.3 below), except for CO_2^+ and the ground state of CO_2. Indeed, the number density of CO_2^+ is simply determined by electrical neutrality in the plasma, i.e. from the calculated densities of the electrons and of the negative and other positive ions. The number density of ground state CO_2 is obtained by subtracting the sum of the number densities of all other species from the total species number density. The latter is determined from the following gas state equation:

$$P = n_e k T_e + \sum n_s k T_g \tag{4}$$

$$N = n_e + \sum n_s \tag{5}$$

where n_e, n_s, k, T_e, T_g and N are the electron number density, the number density of the various other species s, the Boltzmann constant, the electron temperature, the gas temperature and the total species number density, respectively. We assume that the local pressure inside the plasma is constant (i.e. equal to atmospheric pressure), while the electron and gas temperature are calculated with equations (10) and (16) below)

The species fluxes $\overrightarrow{G_s}$ in equation (3) are calculated from the drift-diffusion approximation. The ion flux is written as follows:

$$\overrightarrow{G_s} = \frac{q_s}{|q_s|}\mu_s n_s \overrightarrow{E_{amb}} - D_s \nabla n_s. \tag{6}$$

The electron flux is

$$\overrightarrow{G_s} = \frac{q_e}{|q_e|}\mu_e n_e \overrightarrow{E_{amb}} - D_e \nabla n_e. \tag{7}$$

The mobility and diffusion coefficient of the electrons are derived from BOLSIG + [35]. For the ions, the mobilities of O_2^+ and CO_2^+ in CO_2 are adopted from [36], and the values for O^- and CO_3^- in CO_2 are taken from [37]. We did not find data of the mobility of O_2^- in CO_2 in the literature, but in [36] it is reported that the mobility of O_2^- in oxygen is 30% lower than the value of O^- in oxygen. However, in our work, we assumed the mobility of O_2^- to be the same as that of the O^- ions, following the treatment of [38]. We checked this approximation and found that it has no influence on the results, because of the low radial electric field. The influence of pressure and gas temperature on the mobilities is taken into account, following the treatment of [39]. The corresponding diffusion coefficients of the ions are calculated using the Einstein relation, where the ratio of diffusion coefficient to mobility is directly proportional to the temperature of the ions. Finally, for the neutral species, the diffusion coefficients are determined using gas kinetic theory by the Chapman–Enskog method, as explained in [40].

The electron energy equation is solved for the average electron energy density $n_e \overline{\varepsilon_e}$:

$$\frac{\partial n_e \overline{\varepsilon_e}}{\partial t} + \nabla \overrightarrow{G_{\varepsilon,e}} = \sigma \vec{E}^2 + n_e \Delta \overline{\varepsilon_{el}} + n_e \Delta \overline{\varepsilon_{inel}} - (n_e \overline{\varepsilon_e} - (n_e \overline{\varepsilon_e})_{bg})F \tag{10}$$

where $\overline{\varepsilon_e}$ is the averaged electron energy, from which the average electron temperature is evaluated as $T_e = (2/3)\overline{\varepsilon_e}$ in eV.

The plasma electric conductivity is defined as:

$$\sigma = e(n_{CO_2^+}\mu_{CO_2^+} + n_{O_2^+}\mu_{O_2^+} + n_{CO_3^-}\mu_{CO_3^-} + n_{O^-}\mu_{O^-} + n_{O_2^-}\mu_{O_2^-} + n_e\mu_e) \tag{11}$$

where e is the elementary charge.

The first term in the right hand side of equation (10) represents the Joule heating term, the second and the third term are the total electron elastic and inelastic collision energy loss terms, respectively, with $\Delta \overline{\varepsilon_{el}}$, $\Delta \overline{\varepsilon_{inel}}$ being negative values, and the last term accounts for the electron energy losses due to convection by the gas flow, as explained in previous section.

The electron energy density flux $\overrightarrow{G_{\varepsilon,e}}$ is expressed as follows

$$\overrightarrow{G_{\varepsilon,e}} = -D_{\varepsilon,e}\nabla(n_e \varepsilon_e) - \mu_{\varepsilon,e}n_e \varepsilon_e \overrightarrow{E_{amb}}. \tag{12}$$

The electron energy mobility is written as:

$$\mu_{\varepsilon,\mathrm{e}} = \frac{5}{3}\mu_{\mathrm{e}}. \tag{13}$$

The electron energy diffusion coefficient is [24]:

$$D_{\varepsilon,\mathrm{e}} = \frac{2}{3}\overline{\varepsilon_{\mathrm{e}}}\mu_{\varepsilon,\mathrm{e}}. \tag{14}$$

The electric field is obtained from the current continuity equation:

$$E = \frac{I}{G} = \frac{I}{\int_0^{r_{\max}} 2\pi r\sigma\,\mathrm{d}r} \tag{15}$$

where $G = \int_0^{r_{\max}} 2\pi r\sigma\,\mathrm{d}r$ is the electrical conductance over the entire arc discharge channel, with σ being the plasma electric conductivity, calculated with equation (11), and $r_{\max}$ is the maximum radius of the arc discharge channel (see figure 1). Note that this electric field is used only for the Joule heating calculation in equation (10) and it does not contribute to the transport of particles and energy, for which the ambipolar electric field in equation (9) is used. The model solves the logarithm of the species densities n_{s} and electron energy density $n_{\mathrm{e}}\overline{\varepsilon_{\mathrm{e}}}$, in order to improve the stability of the calculations.

The gas heat transfer equation is solved for the gas translational temperature T_{g}:

$$\rho C_{\mathrm{p}}\frac{\partial T_{\mathrm{g}}}{\partial t} = \nabla k_{\mathrm{t}}(\nabla T_{\mathrm{g}}) + P_{\mathrm{e,el}} - \sum_j R_j\Delta H_j$$
$$- (\rho C_{\mathrm{p}}T_{\mathrm{g}} - (\rho C_{\mathrm{p}}T_{\mathrm{g}})_{\mathrm{bg}})F \tag{16}$$

where $\rho = \sum_{\mathrm{s}} m_s n_s$ is the total mass density of the ionized gas (i.e. the sum of the mass densities of all heavy species).

The first, second, third and fourth term in the right hand side of equation (16) represent heat conduction, the power transferred from the electrons to the heavy particles by elastic collisions (corresponding to the second term of the right-hand side of equation (10)), the power consumed by the heavy particle reactions (with ΔH_j being positive or negative in case of heat consumed or released in the reaction j), and the heat loss caused by the convective cooling effect, as explained in previous section. R_j is the reaction rate of reaction j, defined as:

$$R_j = k_j\prod_l n_l \tag{17}$$

where k_j is the rate coefficient of reaction j, and n_l stands for the number density of the various reactants l in this reaction.

The thermal conductivity of a gaseous mixture k_t is evaluated by the Chapman–Enskog method [40]. The specific heat at constant pressure C_{p} is determined by

$$C_{\mathrm{p}} = \frac{\gamma}{\gamma - 1}\frac{k}{M} \tag{18}$$

where k and M are the Boltzmann constant and the molar weight of the gaseous mixture, respectively.

The specific heat ratio of the gaseous mixture, γ, is determined as

$$N\frac{\gamma}{\gamma - 1} = \sum_{\mathrm{s}} n_{\mathrm{s}}\frac{\gamma_{\mathrm{s}}}{\gamma_{\mathrm{s}} - 1} \tag{19}$$

where γ_{s} is the specific heat ratio of species *s*.

As in previous work from our group [25], the specific heat ratio is taken as 1.67 for the atomic species and 1.40 for the diatomic molecules (CO and O_2). For CO_2, we only have to take into account the heat capacity due to translational and rotational degrees of freedom, as well as the vibrational symmetric mode levels that are not described by an individual species. Details can be found in [25].

The above set of 1D radially-dependent equations for the various species densities, the electron and gas temperature and the ambipolar electric field in the CO_2 plasma at atmospheric pressure is solved by means of the COMSOL Multiphysics software [41] in a cylindrical frame with maximum radius $r_{\max} = 2\,\mathrm{mm}$. At the boundary of $r_{\max} = 2\,\mathrm{mm}$, the same values as the background values for the solution variables are assumed (see above). In order to properly initiate the discharge within the core region of the arc, and not at another location, we have to apply a perturbation. More specifically, we apply the following artificial gas temperature distribution:

$$T(r) = 300\,(\mathrm{K}) + 100\,(\mathrm{K})\exp(-r^2/(2*(0.5\,(\mathrm{mm}))^2)). \tag{20}$$

Additionally, we use the concentrations of CO_2 in the ground state and the various excited levels following a Maxwellian distribution as the initial values.

2.3. Chemistry set considered in the model

The chemistry set is based on the full chemistry set developed by Kozák and Bogaerts [24, 25] which gives reasonable agreement with experimental work for a microwave plasma, but it is somewhat reduced to only include the most important species and processes, while still accounting for the full vibrational kinetics, as presented by Berthelot and Bogaerts [31]. However, in contrast to [31], we also take into account the O_2^+ ions, which become increasingly important at higher CO_2 conversion. The list of species considered in the model is shown in table 1. The meaning of the CO_2 vibrational levels, i.e. $CO_2(v_a–v_d)$ and $CO_2(v_1–v_{21})$, is explained in detail in previous papers from our group [24, 25, 31]. The reaction chemistry can be found in tables 2–5. Recently we investigated the role of the electron impact dissociation cross section of CO_2 [42], and following this recommendation, we take into account two electronic excitations for CO_2, with threshold energies at 7.0 eV and 10.5 eV, respectively, but the 7.0 eV threshold energy process is considered as a dissociative channel. For this reason, only one CO_2 electronically excited level is listed in table 1.

As indicated in table 2, the rate coefficients of most electron impact reactions are calculated from the cross sections by means of an external Boltzmann solver, i.e. BOLSIG + [35]. The latter calculates the electron energy distribution function (EEDF) for given values of electric field, based on all electron impact reactions included in the model. This is a necessary

Table 1. Overview of the species included in the model.

Neutral ground state species		CO_2, CO, C, O_2, O
Charged species		CO_2^+, O_2^+, CO_3^-, O^-, O_2^-, e^-

Excited states	Energy level	State
$CO_2(v_a)$	0.083 eV [43]	(010)
$CO_2(v_b)$	0.167 eV [43]	$(020) + (100)$
$CO_2(v_c)$	0.252 eV [43]	$(030) + (110)$
$CO_2(v_d)$	0.339 eV [43]	$(040) + (120) + (200)$
$CO_2(v_1{-}v_{21})$	Anharmonic oscillator [44]	$(00n)$
$CO_2(e1)$	10.5 eV [43]	$^1\sum_u^+$
$O_2(v_1{-}v_3)$	0.19 eV, 0.38 eV, 0.57 eV [45]	

Table 2. Electron impact reactions included in the model.

Process	Reaction	Rate coefficient	Reference	Note
Elastic collision	$e^- + CO_2 \rightarrow e^- + CO_2$	EEDF	[43]	a
Ionization	$e^- + CO_2 \rightarrow e^- + e^- + CO_2^+$	EEDF	[43]	a
Dissociative attachment	$e^- + CO_2 \rightarrow O^- + CO$	EEDF	[43]	b
Dissociation	$e^- + CO_2 \rightarrow e^- + CO + O$	EEDF	[43]	b,d
Electronic excitation	$e^- + CO_2 \rightarrow e^- + CO_2e1$	EEDF	[43]	a
Vibrational excitation)	$e^- + CO_2 \rightarrow e^- + CO_2v_a$	EEDF	[43]	
Vibrational excitation	$e^- + CO_2 \rightarrow e^- + CO_2v_b$	EEDF	[43]	
Vibrational excitation	$e^- + CO_2 \rightarrow e^- + CO_2v_c$	EEDF	[43]	
Vibrational excitation	$e^- + CO_2 \rightarrow e^- + CO_2v_d$	EEDF	[43]	
Vibrational excitation	$e^- + CO_2 \rightarrow e^- + CO_2v_i$	EEDF	[43]	$i = 1{-}21$ c
Elastic collision	$e^- + CO \rightarrow e^- + CO$	EEDF	[46]	
Dissociation	$e^- + CO \rightarrow e^- + C + O$	EEDF	[46]	
Dissociative attachment	$e^- + CO \rightarrow C + O^-$	EEDF	[46]	
Elastic collision	$e^- + O_2 \rightarrow e^- + O_2$	EEDF	[45]	a
Dissociation	$e^- + O_2 \rightarrow e^- + O + O$	EEDF	[45]	b
Ionization	$e^- + O_2 \rightarrow e^- + e^- + O_2^+$	EEDF	[45]	a
Dissociative attachment	$e^- + O_2 \rightarrow O + O^-$	EEDF	[45]	b
Attachment	$e^- + O_2 + M \rightarrow M + O_2^-$	EEDF	[45]	a
Vibrational excitation	$e^- + O_2 \rightarrow e^- + O_2v_i$	EEDF	[45]	$i = 1, 2, 3$
Attachment	$e^- + O + M \rightarrow M + O^-$	1.00×10^{-31}	[47]	
Electron–ion recombination	$e^- + CO_2^+ \rightarrow CO + O$	$2.0 \times 10^{-5}T_e^{-0.50}/T_g$	[48]	
Electron–ion recombination	$e^- + CO_2^+ \rightarrow C + O_2$	$3.94 \times 10^{-7}T_e^{-0.40}$	[49]	
Electron–ion recombination	$e^- + O_2^+ + M \rightarrow O_2 + M$	1.00×10^{-26}	[50]	
Electron–ion recombination	$e^- + O_2^+ \rightarrow O + O$	$6.0 \times 10^{-7}T_e^{-0.50}T_g^{-0.50}$	[48]	

a Same cross section used for reactions of CO_2v_i, and idem for O_2v_i.
b Cross section also used for reactions of CO_2v_i, and for O_2v_i, but modified by lowering the energy threshold by the excited state energy.
c Cross section also used for reactions of CO_2v_i, but scaled and shifted in energy using Fridman's approximation [22].
d Dissociation through electron impact excitation with 7.0 eV threshold.
Note: Most rate coefficients are calculated from the cross sections and the electron energy distribution function, calculated in BOLSIG+ (see text below), as indicated in the table by EEDF. Some rate coefficients (e.g. for electron–ion recombination) are directly adopted from literature. They are expressed in $(cm^3 \cdot s^{-1})$ or $(cm^6 \cdot s^{-1})$ for two-body and three-body reactions, respectively. T_e is in eV and T_g is in K.

approximation, as a 1D model solving the Boltzmann equation would be computationally expensive. From the calculated EEDF, the rate coefficients k_i can be obtained by:

$$k_i = \sqrt{\frac{2e}{m}} \int_0^\infty \sigma_i \varepsilon f(\varepsilon) d\varepsilon \qquad (21)$$

where the parameters e, m, ε, and σ_i are the elementary charge, the electron mass, electron energy and electron impact cross section of the process i, respectively, and $f(\varepsilon)$ is the EEDF.

2.4. Level lumping

Following the treatment of [31], the chemistry model presented in previous section, with all vibrational levels of the asymmetric mode taken into account, is reduced by grouping the asymmetric mode vibrational levels ($CO_2(v_{1-21})$ in table 1) into a number of lumped levels. This is done to check the validity of this level lumping strategy for a gliding arc, and to allow this method to be used in 2D or 3D models in the future. The symmetric mode vibrational levels (i.e. $CO_2 (v_a, v_b, v_c, v_d)$ in table 1)

Table 3. Ion reactions included in the model.

Process	Reaction	Rate coefficient	Reference
Recombination[a]	$O^- + CO_2 + M \rightarrow CO_3^- + M$	9.0×10^{-29}	[48]
Electron detachment	$O^- + CO \rightarrow CO_2 + e^-$	5.5×10^{-10}	[49]
Electron detachment	$CO_3^- + CO \rightarrow 2CO_2 + e^-$	5.0×10^{-13}	[48]
Recombination	$CO_3^- + CO_2^+ \rightarrow 2CO_2 + O$	5.0×10^{-7}	[48]
Electron detachment[a]	$O^- + M \rightarrow e^- + O + M$	4.0×10^{-12}	[51]
Electron detachment	$O^- + O \rightarrow e^- + O_2$	2.3×10^{-10}	[52]
Charge transfer	$O_2^- + O \rightarrow O^- + O_2$	3.3×10^{-10}	[50]
Electron detachment	$O_2^- + O_2 \rightarrow O_2 + O_2 + e^-$	2.18×10^{-18}	[50]
Electron detachment[a]	$O_2^- + M \rightarrow O_2 + M + e^-$	$2.70 \times 10^{-10}(T_g/300)^{0.50} \exp(-5590/T_g)$	[49]
Charge transfer	$O + CO_3^- \rightarrow CO_2 + O_2^-$	8.0×10^{-11}	[48]
Recombination	$O_2^- + CO_2^+ \rightarrow CO + O_2 + O$	6.0×10^{-7}	[48]
Charge transfer	$O_2 + CO_2^+ \rightarrow CO_2 + O_2^+$	5.3×10^{-11}	[53]
Charge transfer	$O + CO_2^+ \rightarrow CO + O_2^+$	1.64×10^{-10}	[53]
Recombination	$O_2^+ + CO_3^- \rightarrow CO_2 + O_2 + O$	3.0×10^{-7}	[48]
Recombination	$O_2^+ + O_2^- \rightarrow O_2 + O_2$	2.0×10^{-7}	[52]
Recombination	$O_2^+ + O_2^- \rightarrow O_2 + O + O$	4.2×10^{-7}	[48]
Recombination[a]	$O_2^+ + O_2^- + M \rightarrow O_2 + O_2 + M$	2.0×10^{-25}	[46]
Recombination	$O_2^+ + O^- \rightarrow O_2 + O$	1.0×10^{-7}	[48]
Recombination	$O_2^+ + O_2^- \rightarrow O_2 + O + O$	2.6×10^{-8}	[52]

[a]*M* represents any neutral species taken into account in the model. The same rate coefficient is used for every species.
Note: The rate coefficients are in $(cm^3 \cdot s^{-1})$ or $(cm^6 \cdot s^{-1})$ for the two-body and three-body reactions, respectively.

Table 4. Vibrational energy transfer reactions included in the model.

Process	Reaction	Rate coefficient	Note	Reference
VT relaxation[a]	$CO_2v_x + M \rightarrow CO_2 + M$	$7.14 \times 10^{-8} \exp(-177/T_g^{-1/3} + 451/T_g^{-2/3})$	$x = a, b, c, d$	[54]
VT relaxation (i)[a,b]	$CO_2v_1 + M \rightarrow CO_2v_a + M$	$0.43 \exp(-407/T_g^{-1/3} + 824/T_g^{-2/3})$		[54]
VT relaxation (ii)[a,b]	$CO_2v_1 + M \rightarrow CO_2v_b + M$	$0.86 \exp(-404/T_g^{-1/3} + 1096/T_g^{-2/3})$		[54]
VT relaxation (iii)[a,b]	$CO_2v_1 + M \rightarrow CO_2v_c + M$	$1.43 \times 10^{-5} \exp(-252/T_g^{-1/3} + 685/T_g^{-2/3})$		[54]
VV′ relaxation	$CO_2v_i + CO_2 \rightarrow CO_2v_{i-1} + CO_2v_x$	$2.13 \times 10^{-5} \exp(-242/T_g^{-1/3} + 633/T_g^{-2/3})$	$x = a, b;$ $i \geqslant 2$	[54]
VV relaxation[c]	$CO_2v_i + CO_2v_j \rightarrow CO_2v_{i-1} + CO_2v_{j+1}$	$1.80 \times 10^{-11} \exp(24.7/T_g^{-1/3} - 65.7/T_g^{-2/3})$	$20 \geqslant j \geqslant 0$ $21 \geqslant i \geqslant 1$	[55, 56]
VT relaxation[a,c]	$O_2v_i + M \rightarrow O_2v_{i-1} + M$	$7.99 \times 10^{-5} \exp(-320/T_g^{-1/3} + 615/T_g^{-2/3})$	$i = 1, 2, 3$	[54]

[a]*M* represents any neutral species taken into account in the model. The same rate coefficient is used for every species.
[b]These reactions are also taken into account for v_i ($i > 1$), but then they are not considered separately, and the rate coefficient is then taken as the sum of (i), (ii) and (iii), leading to level CO_2v_{i-1}, because for the higher levels, no individual symmetric mode levels are included in the model. See Kozák and Bogaerts [24, 25] for more information.
[c]v_0 means the ground state of CO_2 or O_2.
Note: The rate coefficients are in $(cm^3 \cdot s^{-1})$ and T_g is in K. The rate coefficients are given for the reaction between ground state and first vibrational level, and they are scaled for the higher transitions.

are not further lumped together. The level lumping method was explained in detail in [31] for a 0D model, so here only the characteristic features needed for the 1D model are presented.

The total number density of the lumped-levels group i, n_{g_i}, can be determined by summation of the number density of all the levels (j) within this group

$$n_{g_i} = \sum_{j \in g_i} n_j \quad i = 1, \dots, l \quad \text{for } l \text{ groups.} \tag{22}$$

Vice versa, from the total number density of the group i, n_{g_i}, the number density of each level within this group can be determined from the VDF $f(E_j, T_i)$ where E_j is the energy of the jth level within group g_i, and T_i is the temperature associated to the group g_i

$$n_{j \in g_i} = n_{g_i} \frac{f(E_j, T_i)}{\sum_{s \in g_i} f(E_s, T_i)}. \tag{23}$$

Table 5. Neutral reactions included in the model.

Reaction	Rate coefficient	ΔH_j (eV)	α	Reference
$CO_2 + M \rightarrow CO + O + M$	$4.39 \times 10^{-7} \exp(-65\,000/T_g)$	5.52	1.0	[2]
$CO_2 + O \rightarrow CO + O_2$	$7.77 \times 10^{-12} \exp(-16\,600/T_g)$	0.35	0.5	[2]
$CO + O + M \rightarrow CO_2 + M$	$8.2 \times 10^{-34} \exp(-1560/T_g)$	−5.52		[47]
$CO + O_2 \rightarrow CO_2 + O$	$1.28 \times 10^{-12} \exp(-12\,800/T_g)$	−0.35	0.5	[2]
$CO_2 + C \rightarrow CO + CO$	1.0×10^{-15}	−5.64		[51]
$O_2 + C \rightarrow CO + O$	3.0×10^{-11}	−5.99		[47]
$CO + M \rightarrow C + O + M$	$1.52 \times 10^{-4} (T_g/298)^{-3.1} \exp(-12800/T_g)$	11.16		[57]
$C + O + M \rightarrow CO + M$	$2.14 \times 10^{-29} (T_g/300)^{-3.08} \exp(-2114/T_g)$	−11.16		[49]
$O + O + M \rightarrow O_2 + M$	$1.27 \times 10^{-32} (T_g/300)^{-1} \exp(-170/T_g)$	−5.17		[58]

Note: The rate coefficients are in $(\text{cm}^3 \cdot \text{s}^{-1})$ or in $(\text{cm}^6 \cdot \text{s}^{-1})$ for the two-body and three-body reactions, respectively. T_g is in K. α is the parameter used in the Fridman approximation to determine the rate coefficients of the same reactions with vibrationally excited CO_2 molecules. See Kozák and Bogaerts [24, 25] for more information ΔH_j (eV) is used to calculate the power released by the heavy particle reactions in equation (16) above.

In our current work, we assume that the vibrational states in each group follow a Maxwellian internal vibrational distribution and hence the number density of the vibrational states within the group g_i can be determined as follows.

$$n_{j \in g_i} = n_{g_i} \frac{\exp(-E_j/kT_i)}{\sum\limits_{s \in g_i} \exp(-E_s/kT_i)}. \quad (24)$$

Similarly, the mean group vibrational energy $\overline{E_{v,g_i}}$ can be obtained:

$$\overline{E_{v,g_i}} = \sum\limits_{j \in g_i} E_j \frac{\exp(-E_j/kT_i)}{\sum\limits_{s \in g_i} \exp(-E_s/kT_i)}. \quad (25)$$

Using the relationships (24) and (25), we can obtain the conservation equation for the total number density of each group i (equation (26)) and the conservation equation for the mean group vibrational energy density (equation (27)).

$$\frac{\partial n_{g_i}}{\partial t} + \nabla \overrightarrow{G_{g_i}} = \sum\limits_{j \in g_i} S_j - (n_{g_i} - (n_{g_i})_{bg}) F \quad (26)$$

$$\frac{\partial n_{g_i} \overline{E_{v,g_i}}}{\partial t} + \nabla \overrightarrow{G_{E_v,g_i}} = \sum\limits_{j \in g_i} E_j S_j - (n_{g_i} \overline{E_{v,g_i}} - (n_{g_i} \overline{E_{v,g_i}})_{bg}) F \quad (27)$$

where $S_j = \frac{\partial n_j}{\partial t}\Big|_{j \in g_i}$ is the source term for each individual level j.

Thus, this level lumping technique allows to replace the continuity equations for the individual levels by the above-mentioned two equations for each group of lumped levels, and thus it reduces the total number of equations to be solved in the model.

The flux of group $\overrightarrow{G_{g_i}}$ and the grouped vibrational energy density flux $\overrightarrow{G_{E,g_i}}$ are written as follows:

$$\overrightarrow{G_{g_i}} = -D_{g_i} \nabla n_{g_i} \quad (28)$$

Table 6. Asymmetric mode vibrational levels included within each group, for the different lumped-levels models developed.

	Group 1	Group 2	Group 3
1G model	1–21	×	×
2G model	1–6	7–21	×
3G model	1–6	7–14	15–21

$$\overrightarrow{G_{E_v,g_i}} = -D_{E_v,g_i} \nabla (n_{g_i} \overline{E_{v,g_i}}). \quad (29)$$

Instead of the level lumping strategy, we can also assume a simple thermal equilibrium between the vibrational temperature and the gas translational temperature, yielding the following description of the VDF:

$$n_j = n_0 \frac{\exp(-E_j/kT_g)}{\sum\limits_{1 \leqslant s \leqslant 21} \exp(-E_s/kT_g)} \quad j = 1, \ldots, 21 \quad (30)$$

with n_0 being the density of the CO_2 ground state. In the results section, we will refer to this as the 'thermal distribution model'.

We found that a careful selection of the levels in each group is crucial to obtain good agreement with the model treating all levels separately. Moreover, our selection of levels within each group is different from the one presented in [31] for the MW plasma. Table 6 shows the levels included within each group in our study, for each of the lumped-levels models developed, i.e. the one-group (1G), two-groups (2G) and three-groups (3G) model. This subdivision was chosen in order to fit the VDF predicted by the individual-levels model. The same groups are considered for all the conditions investigated in this work, in order to make the lumped-levels models as general as possible.

3. Results and discussion

In section 3.1, we will present the calculation results of the 1D gliding arc model under both quasi-steady state and transient conditions, corresponding to a DC and AC gliding arc,
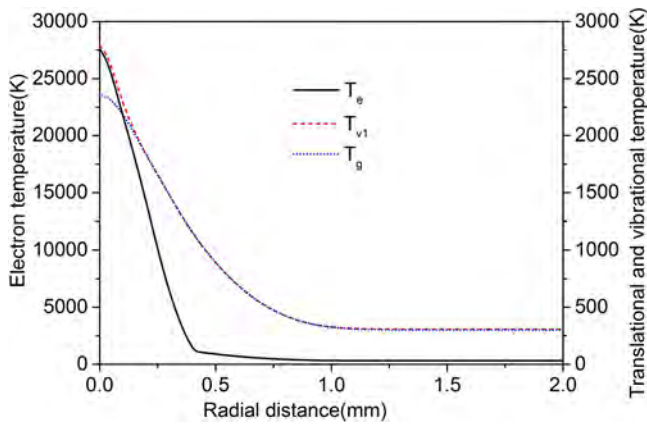
Figure 2. Radial distributions of the electron temperature T_e (left axis), the vibrational temperature of the asymmetric mode $T_{v1}(CO_2)$ and the gas (translational) temperature T_g (right axis) in the CO_2 gliding arc, at a discharge current of 10 mA, and a characteristic frequency of convective cooling of 2.5 kHz.

respectively. If not specifically indicated, a characteristic frequency for convective cooling of 2.5 kHz will be assumed. The quasi-steady state corresponds to a constant electrical current imposed on the discharge channel (see equation (15)), like in a DC case, i.e. the calculations are performed until the discharge properties reach a quasi-steady state, where a dynamic balance between the production and loss of the plasma species and energy is reached and the discharge properties will not vary with time anymore. We should point out that the loss of the plasma species and energy includes the contributions from the chemical reactions, as well as from the transport phenomena, including both the diffusion and drift, as well as convective losses due to the relative velocity of the gas flow with respect to the arc and the gliding arc elongation.

The transient condition corresponds to an AC gliding arc, and uses an alternating sinusoidal current, $I = 25\sin(2\pi 50 t)$ (mA), for which only one half cycle of the voltage source, for a time duration of 10 ms starting at $t = 0$ ms, is considered. It should be mentioned that the back-breakdown and re-ignition phenomena of the gliding arc [15], which can cause the previously established discharge channel to extinguish, followed by the formation of a new arc at a new location in a time less than half of the voltage period (i.e. 10 ms), is not considered in our model.

In section 3.2, we will investigate the role of electrons, ions and neutrals in the splitting (and formation) of CO_2 in the gliding arc. In section 3.3, the influence of different values for the characteristic frequency of convective plasma cooling on the discharge behavior will be discussed. Finally, in section 3.4, we will present the effectiveness of lumping the CO_2 vibrational levels for modelling CO_2 conversion in a gliding arc, by comparing the results for different groups of lumped levels with the results obtained by the full model treating all individual excited levels separately.

3.1. Typical gliding arc discharge characteristics

3.1.1. Quasi-steady state condition. Figure 2 illustrates the radial distributions of the electron temperature T_e, the
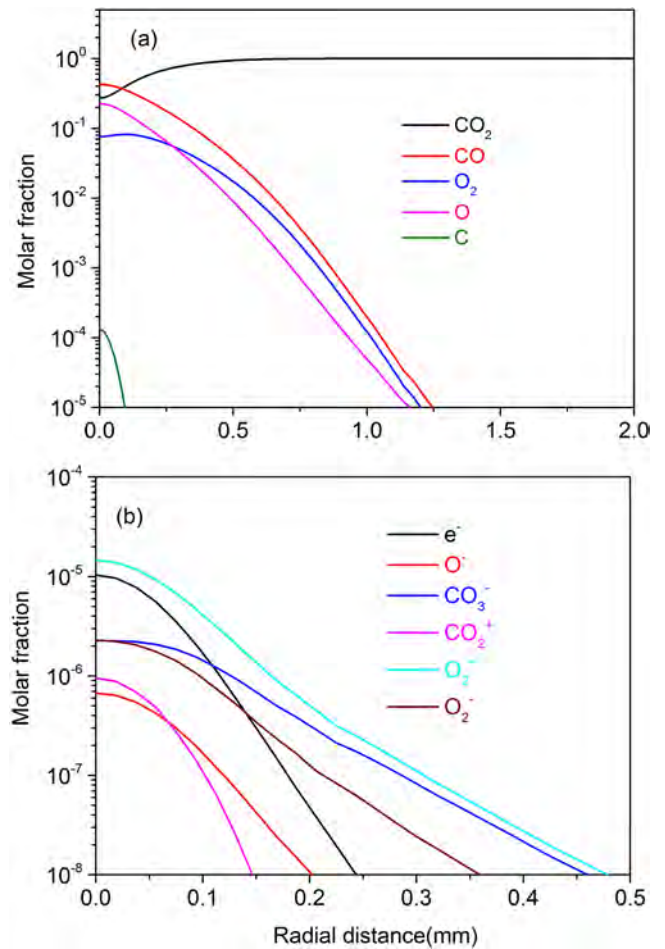

Figure 3. Radial distributions of the molar fractions of the neutral species (a) and charged species (b) in the CO_2 gliding arc, at the same conditions as in figure 2.
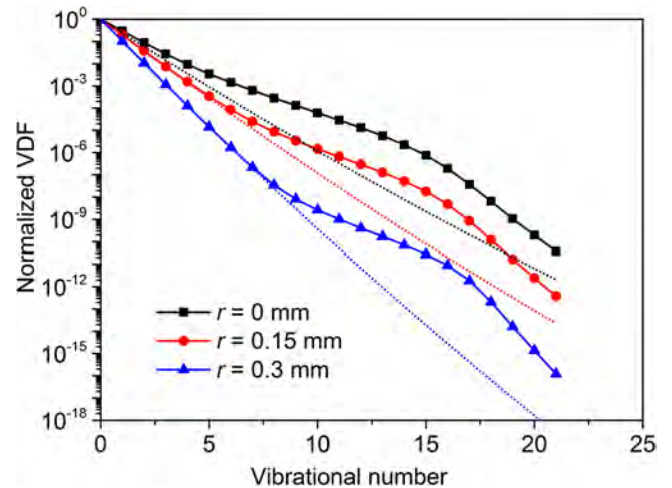
Figure 4. VDFs at different radial positions in the discharge channel, at the same conditions as in figure 2. The dotted lines show the thermal distribution assuming the vibrational temperature equal to the gas temperature.

vibrational temperature of the asymmetric mode $T_{v1}(CO_2)$ and the gas (translational) temperature T_g at quasi-steady state conditions, and at a discharge current of 10 mA, and a characteristic frequency of convective cooling of 2.5 kHz. Note that
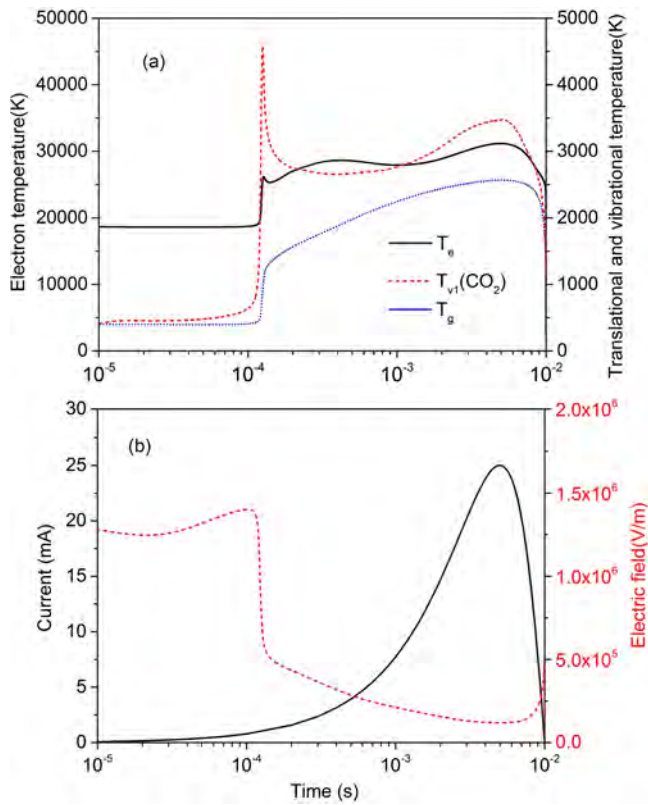
Figure 5. Time evolution of the electron temperature T_e (left axis), the vibrational temperature of the asymmetric mode $T_v(CO_2)$ and the gas (translational) temperature T_g (right axis) (a), as well as the discharge current ($I = 25\sin(2\pi 50t)$ mA) and the electric field (dashed line) (b) at the centre of the arc, at a characteristic frequency of convective cooling of 2.5 kHz.

the VDF of the asymmetric mode is not characterized by a Maxwellian distribution, as will be illustrated in below, and therefore it has more than one vibrational temperature. The vibrational temperature plotted in figure 2 applies to the first part of the VDF, and is calculated as

$$T_{v_1}(CO_2) = -\frac{E_{v_1}}{k \ln(n_{v_1}/n_0)} \qquad (31)$$

where $E_{v_1}/k = 3377$ K is the energy of the first level of the asymmetric mode ($CO_2 v_1$) and n_{v1} and n_0 are the densities of $CO_2 v_1$ and the CO_2 ground state, respectively. Thus, strictly speaking, we should call this $T_{v_1}(CO_2)$, as indicated in the formula.

The temperatures all reach their maximum in the center of the arc, as is logical, and they drop significantly as a function of radial position. The electron temperature reaches a maximum of 27 600 K (or 2.4 eV) in the center of the arc, but it drops significantly as a function of rising distance in the first 0.5 mm, followed by a slower decay to thermal values at a radial distance of about 1.0 mm from the center. The gas temperature is at maximum about 2360 K in the center of the arc, while the vibrational temperature of the asymmetric mode reaches a maximum value of 2788 K in the center of the arc. From the comparison between these temperatures, it is clear that the gliding arc is far from thermal equilibrium, as the electron temperature is about 10 times higher than the gas temperature and vibrational temperature. The vibrational

temperature and gas temperature, on the other hand, are very comparable to each other, except in the center of the arc, where the vibrational temperature is somewhat higher.

The molar fractions of the major neutral and charged species occurring in the CO_2 gliding arc are plotted as a function of radial position in figure 3, at the same conditions as in figure 2. It is clear that CO_2 is the major component in the plasma, except at the center of the arc, where the molar fraction of CO_2 is lower than the fraction of CO, and comparable to the molar fraction of O. This indicates that the majority of CO_2 is split here into CO and O, due to the electron, vibrational and gas temperature, as illustrated in figure 2 above. Moreover, part of the O atoms have recombined into O_2 molecules. However, the molar fractions of CO, O and O_2 drop quickly as a function of radial position, indicating that most of the CO_2 splitting takes place in the center of the arc, as will be explained below. The molar fraction of C atoms is very low, even in the center.

The same is true for the molar fractions of the various ions, which are at maximum 10^{-5}, and they also clearly drop upon larger radial distance from the center of the arc. Also the electron molar fraction is at maximum 10^{-5}, indicating that the CO_2 plasma is only weakly ionized, even in the center of the arc. The major positive ions are the O_2^+ ions, while the CO_3^- ions are the major negative ions, and they are even more important (although still with very low molar fractions) than the electrons, except in the center of the arc.

In figure 4, the normalized VDFs are plotted, obtained at different radial positions, i.e. $r = 0$ mm, 0.15 mm and 0.3 mm, which are characterized by gas temperatures of 2360 K, 2020 K and 1484 K, respectively. The thermal distributions, based on a vibrational temperature being equal to the gas temperature at that position, are also plotted for comparison. In a Maxwellian energy distribution, the vibrational temperature is given by the slope of the VDF (on a logarithmic scale). It is clear, however, from this figure that we can define different vibrational temperatures, based on the different slopes in the VDFs, which correspond to different groups within the vibrational level population. This will be used for the level-lumping strategy, illustrated in section 3.4 below.

In the arc centre, the levels (v_1–v_6) have a somewhat uniform vibrational temperature of 3017 K, as a result of the VT and VV relaxation processes. This value for the whole group is slightly higher than the vibrational temperature of $T_{v_1}(CO_2)$ given by equation (31) (see figure 2 above). This can be explained because the levels (v_2–v_6) are slightly overpopulated. Both this first part of the VDF, as well as the second part of the VDF (v_7–v_{14}), are clearly in non-equilibrium with the gas temperature, because their vibrational temperatures (around 3017 K and 4076 K for the levels (v_1–v_6) and (v_7–v_{14}), respectively) are higher than the gas temperature (2358 K). Finally, the levels (v_{15}–v_{21}) have a lower vibrational temperature (1593 K) than the gas temperature (2358 K). However, these high vibrational levels are still overpopulated when we compare them with the VDF obtained by the thermal equilibrium distribution, assuming the vibrational temperature equal to the gas temperature (see thin dotted line in figure 4). This overpopulation is mainly caused by electron impact vibrational excitation.
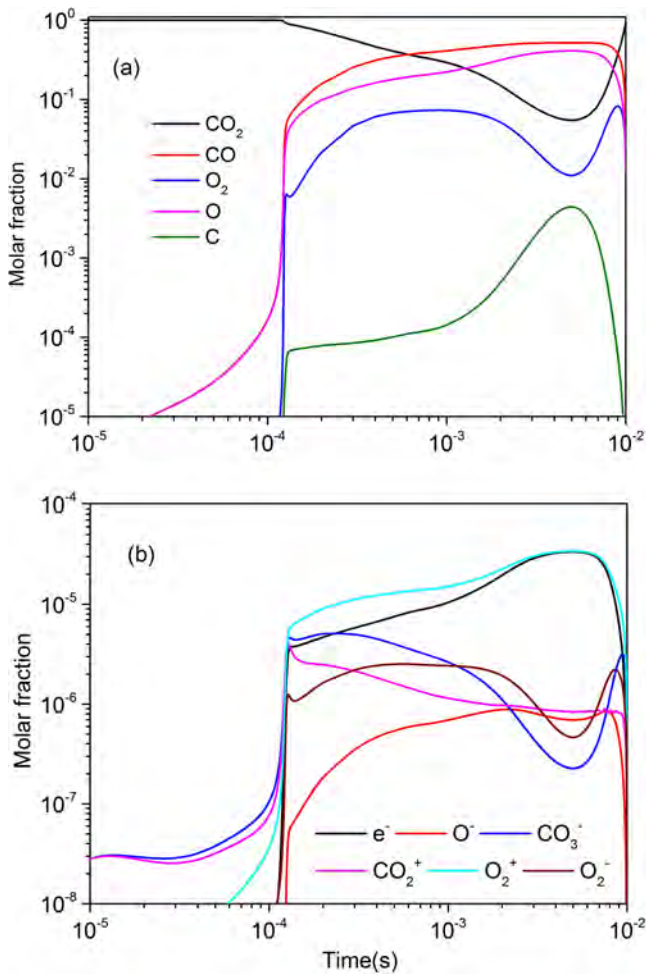
Figure 6. Time evolution of the molar fractions of the neutral species (a) and charged species (b) at the center of the arc, at the same conditions as in figure 5.

With increasing radial distance, the first vibrational levels (v_1–v_6) gradually get close to thermal equilibrium, with a vibrational temperature of about 2081 K at $r = 0.15$ mm and 1484 K at $r = 0.3$ mm. For the latter location, the levels (v_{15}–v_{21}) have a vibrational temperature close to the gas temperature. However, as mentioned above, we cannot say that the vibrational levels within this group reach an equilibrium state, because they are still overpopulated. Furthermore, the vibrational temperature of the levels (v_7–v_{14}) decays only slowly with rising radial distance, and reaches values of 3840 K at $r = 0.15$ mm and 3227 K at $r = 0.3$ mm, thus clearly higher than the gas temperature at these locations, indicating that the vibrational states may have a great influence on the CO_2 conversion. Further analysis of the role of the vibrational kinetics on the CO_2 conversion will be presented in section 3.2 below.

3.1.2. Transient condition. In order to understand the time behavior of the plasma characteristics in the CO_2 gliding arc operating in AC mode, we plot in figure 5 the time evolution of the electron temperature, vibrational temperature of the asymmetric mode and gas (translational) temperature, as well as of the discharge current and electric field, at the centre of the arc and at a current $I = 25\sin(2\pi 50t)$ mA and a characteristic frequency of convective cooling of 2.5 kHz.

Up to $t = 10^{-4}$ s, i.e. when the gas breakdown takes place, the electron temperature is around 18 000 K, and the gas temperature and vibrational temperate are very low (i.e. around the initial value of 400 K). The electric field is gradually increasing to the critical breakdown field, i.e. around 1.4×10^6 V m^{-1} (corresponding to a reduced critical breakdown field of 76 Td at the conditions under study). These conditions correspond to the stage before the ignition of the gliding arc. At $t = 10^{-4}$ s, once the arc is ignited by the electrical breakdown, the three different temperatures suddenly rise, while the electric field shows a sharp drop. Indeed, within the breakdown channel, the abrupt increase of the electron number density during the breakdown (see below) can explain the increasing electron temperature (enhanced Joule heating effect) as well as the rise in vibrational temperature (enhanced electron impact vibrational excitation). With increasing population of the vibrational states, the vibrational energy will partially be transferred to the gas by V–T relaxation, because at atmospheric pressure, the typical characteristic time for V–T relaxation in CO_2 is very short (around 10^{-5} s) [24]. Thus, the gas temperature rises, while the vibrational temperature slightly drops.

At later times, up to $t = $ ca. 5×10^{-3} s, the three temperatures gradually increase further with the rising discharge current (see figure 5(b)), and they reach their maximum values at $t = 5 \times 10^{-3}$ s, when the peak current is reached. The electron temperature does not rise significantly, and stays more or less constant around 25 000–30 000 K, while the vibrational and gas temperature reach a maximum of about 3300 K and 2500 K, respectively. These values are similar to the values obtained at quasi-steady state (see figure 2 above). After $t = 5 \times 10^{-3}$ s, the current, and hence also the electron, vibrational and gas temperature decrease until 10^{-2} s, when the arc extinguishes because the current crosses zero (i.e. end of one half cycle of the AC current), after which this temporal behaviour will be repeated during the next half cycle in a new discharge channel, starting from the shortest gap separation. The electric field, after a sudden drop to 6×10^5 V m^{-1} when the gliding arc is ignited, continues to drop to values of 10^5 V m^{-1} at 5×10^{-3} s upon increase of the arc current, followed by a small rise again when the current is decreasing. This can be explained from equation (15). Indeed, upon rising electric current, the electric conductance (G) increases more than the current, because the electron number density experiences a rapid increase (see below). Hence, this yields a decreasing electric field upon rising current. Vice versa, when the current decreases after $t = 5 \times 10^{-3}$ s, the electric conductance drops more than the current and hence this leads to a slight increase of the electric field, until the arc is extinguished and the electric field suddenly drops to zero because the current reaches zero (see equation (15)). A similar behaviour is also observed in experimental investigations of an AC argon gliding arc [59]. Thus, this behaviour is not specific for our model conditions but it is a more general trend in gliding arc discharges. When the old gliding arc extinguishes, a new gliding arc will be ignited, not in the residual plasma channel of previous half cycle, but in a location at the shortest gap separation of the reactor, where the initial conditions are completely the same
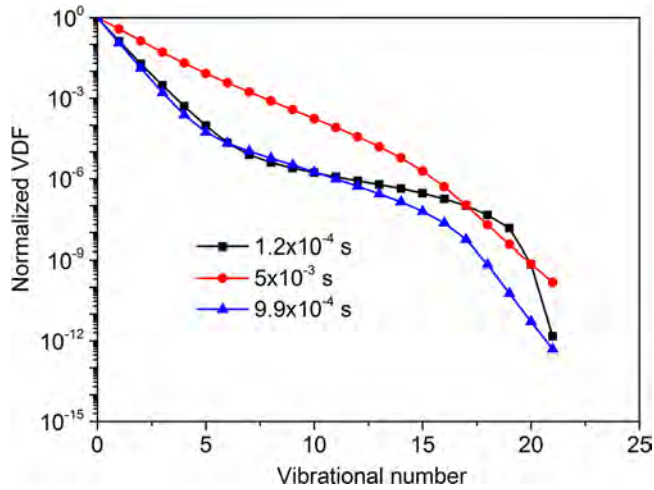
Figure 7. VDFs at $t = 1.2 \times 10^{-4}$ s (black curve), 5×10^{-3} s (red curve) and 9.9×10^{-3} s (blue curve), which correspond to the time of gliding arc discharge initiation, the time of the peak current and of the arc extinction stage, respectively (see figure 5(b) above), at the same conditions as in figure 5.

for different repeated cycles. Thus, the temporal profiles of the temperatures will look the same, although the temperature at the start of this new half cycle will be somewhat different from the value obtained at the end of the previous half cycle, because the previous arc has moved in the meantime to a location with larger gap separation (accounted for in the model by the convective cooling; see section 2.1 above).

Figure 6 illustrates the time-evolutions of the molar fractions of the various neutral and charged species in the center of the arc, at the same conditions as in figure 5. The CO_2 molar fraction is equal to 1 before the arc is formed (i.e. $t = 10^{-4}$ s), but it starts decreasing gradually as a function of time when the current in the arc rises (see figure 5(b) above), up to a value of 0.06 at $t = 5 \times 10^{-3}$ s, indicating that CO_2 is gradually converted into CO, O and O_2. Indeed, the molar fractions of these species increase dramatically at $t = 10^{-4}$ s, and continue to increase until $t = 5 \times 10^{-3}$ s, when the arc current and hence the various temperatures reach their maximum values (see figure 5 above). The molar fraction of O_2, however, starts to drop after $t = 10^{-3}$ s, because the higher discharge current and hence electron number density, as well as the higher plasma temperature, will enhance the splitting rate of O_2 into O atoms. At later times, the discharge current and hence the temperatures start to drop, so the CO_2 conversion gradually decreases until the arc is extinguished. In general, some recombination of CO and O into CO_2 occurs again. Moreover, due to diffusion and convection as a result of the difference between gas flow and arc velocity, some background CO_2 will enter the discharge channel, while a fraction of the dissociation products of CO_2 will leave the discharge channel. This can explain why the CO_2 molar fraction rises again at the end of the half cycle, and the CO and O molar fractions drop. The ratio of the molar fractions of CO to CO_2 integrated over the entire half cycle is 0.28%. However, this is not equal to the overall plasma conversion, because both diffusion and convection will continuously transport CO_2 into the discharge channel, and dissociation products out of the discharge channel, as mentioned above. Because we do not consider the exact flow rate and the reactor geometry in our 1D model, a realistic evaluation of the overall plasma conversion is not possible here.

The molar fractions of the C atoms, and of the various ions and the electrons, are much lower, but they also exhibit a sharp increase at $t = 10^{-4}$ s, when the arc is ignited by the electrical breakdown. The O_2^+ ions are again clearly the dominant positive ions, while the CO_3^- ions are again the major negative ions. The molar fraction of the latter is as high as the electron molar fraction in the beginning of the arc, but it starts decreasing with time, due to the increasing current, because the destruction rate of CO_3^- ions, mainly upon reaction with O atoms, forming CO_2 and O_2^- ions, increases as a result of the rising concentration of O atoms (see figure 6(a)). The electron and O_2^+ molar fractions, however, continues to increase as a function of time, as they follow more or less the time-evolution of the electrical current (see figure 5(b)), and they reach a maximum of about 3.4×10^{-5} at $t = 5 \times 10^{-3}$ s. At later times, the molar fractions of O_2^+ ions and electrons decrease with decreasing current until the arc extinguishes, and the next half cycle starts.

To the best of our knowledge, detailed information about the discharge characteristics including the plasma density and plasma temperatures of a gliding arc discharge for pure CO_2 in classical gliding arc reactors, which corresponds to the condition considered in our current work, has not been reported in the literature. The lack of plasma parameters by experimental work for pure CO_2 in classical gliding arc reactors makes it difficult to validate our model by direct comparison under specific conditions. However, our calculated values for plasma density and plasma temperature are comparable with experimental data from literature, on gliding arc reactors using molecular gases (nitrogen and air) and gaseous mixtures containing CO_2. To be more specific, a literature review shows that the typical gliding arc parameters achieved from experiments are 10^{17}–10^{20} m^{-3} for the electron number density, 1000–4000 K for the gas temperature, up to around 8000 K for the vibrational temperature and 1.0–3.0 eV for the electron temperature [13, 60–65]. Indeed, for a gliding arc in air, Czernichowski *et al* [13] reported values for a plasma density of 10^{18}–10^{19} m^{-3}, a gas temperature of 1000–2600 K and a vibrational temperature of 2200–3900 K, for a diverging electrodes reactor at a current of 130 mA. Gangoli *et al* report values for the rotational (gas) temperature of 2200–2500 K and for the vibrational temperature of 3200–3700 K over the same range of currents (30–200 mA) for a magnetically stabilized air gliding arc discharge [60], and an electron number density of 1.3×10^{19} m^{-3} with a current of 40 mA was obtained in [61]. Zhu *et al* [62] reported values for the gas temperature of about 1100 K, and for the rotational and vibrational temperature of about 3600 K and 6700 K, respectively, for a diverging electrodes gliding arc reactor. Wu *et al* [63] experimentally obtained values for the rotational and electron excitation temperature of approximately 1100–1200 K and 1.1–1.7 eV, respectively, using a rotating gliding arc reactor for a mixture of CH_4/CO_2. Zhao *et al* [64] reported values for
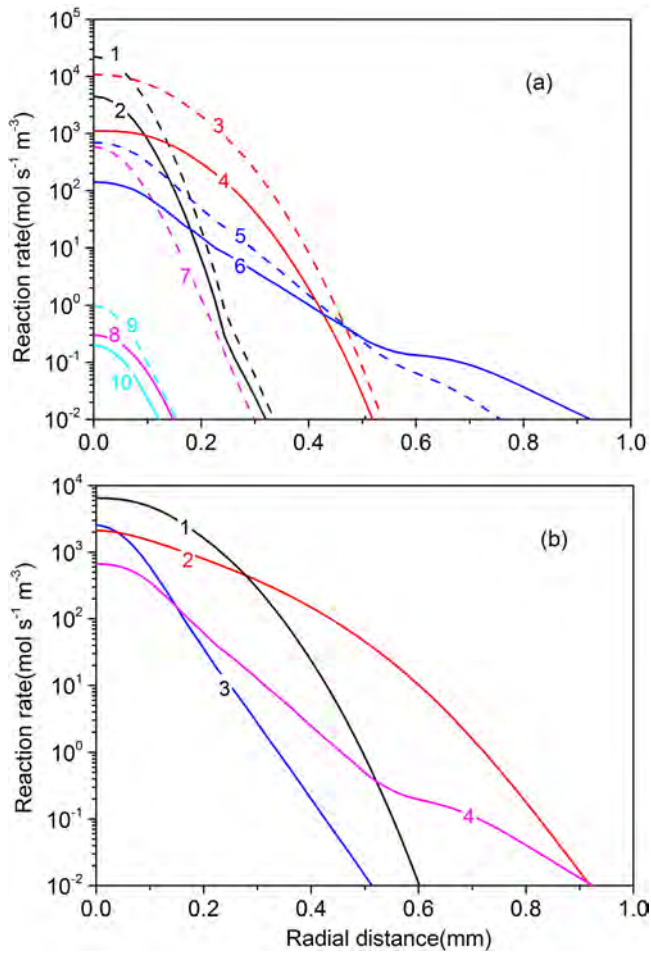
Figure 8. Radial distributions of the reaction rates for CO_2 loss (a) and formation (b) by the most important processes for the quasi-steady state condition, at the same conditions as in figure 2. The numbers of the curves correspond to the reactions listed in tables 7 and 8, for the CO_2 loss and formation mechanisms, respectively. The reactions from the CO_2 vibrational levels are indicated with dashed lines in (a), while the reactions with the CO_2 ground state are plotted with solid lines.

the vibrational temperature of 2500–5500 K and for the rotational temperature of 500–2500 K in a kilohertz AC nitrogen gliding arc. Another measurement was made by Nunnally [65] in a non-equilibrium gliding arc 'tornado' discharge using CO_2 doped with 1% N_2 at a flow rate of 10 lpm and a power of 200 W. By comparing the theoretical and experimentally measured spectra for the N_2 system, the rotational gas temperature was determined to be 2700 K $\pm$ 50 K, while the vibrational temperature was estimated to be approximately 6000 K. Our calculated values of the plasma parameters (i.e. electron number density up to around 10^{20} m^{-3}, gas temperature up to about 2600 K, vibrational temperature up to around 4500 K and electron temperature up to 2.4 eV) thus correspond well to the experimental data for low current atmospheric pressure gliding arc discharges, although it should be mentioned that it is not easy to compare different gliding arc setups with different reactor geometries and discharge conditions.

In figure 7, the normalized VDFs are plotted, obtained at $t = 1.2 \times 10^{-4}$ s, 5×10^{-3} s and 9.9×10^{-3} s, which correspond to the time of discharge initiation, the time of the peak

current and of the arc extinction stage, respectively. During the very short discharge initiation stage at around $t = 1.2 \times 10^{-4}$ s, when the gas temperature is low (475 K; see figure 5(a) above) and there is strong non-equilibrium, the VDF is characterized by three distinct groups of vibrational levels, with different vibrational temperatures, as is clear from the three different slopes. Except for the two highest vibrational levels (v_{20}–v_{21}), which are not much excited due to their high excitation threshold level, the other vibrational levels have a significant population. The vibrational temperature of the first group of levels (v_1–v_6) is around 1733 K, which is clearly higher than the gas temperature of 475 K. The second group of levels (v_7–v_{14}) is characterized by a very high vibrational temperature (around 7026 K, i.e. much higher than the gas temperature), and thus, these levels are significantly overpopulated compared to the Maxwellian distribution following the lower levels. This is attributed to the efficient electron impact excitation to these levels after the electrical breakdown, when the electron number density and electron temperature increases significantly.

At $t = 5 \times 10^{-3}$ s, corresponding to the maximum discharge current and hence the maximum gas temperature in the arc (i.e. around 2600 K; see figure 5(a) above), the population of the levels (v_1–v_{14}) decreases gradually with a more or less constant slope, thus characterized by a somewhat uniform vibrational temperature of about 3500 K, as a result of the VT and VV relaxation processes. Hence, the vibrational temperature is about 900 K higher than the gas temperature, as was also clear from figure 5(a) above. In contrast, the highest levels (v_{15}–v_{21}) have a lower vibrational temperature (1729 K), which can be explained by the high dissociation rate of the highly excited vibrational CO_2 levels upon collision with other heavy particles, i.e. $CO_2 v_i + M \rightarrow CO + O + M$, with M being any type of molecule.

In the arc extinction stage, the current rapidly drops to zero while the electric field slightly rises again (see figure 5(b)) and the temperatures drop again (see figure 5(a)). The VDF is again characterized by three different groups of levels, with distinct vibrational temperatures. The vibrational temperature of the first group is again lower (i.e. around 1573 K), because electron impact vibrational excitation becomes less important due to the drop of the electron number density within the discharge channel when the discharge current decreases towards zero (see figure 5(a)). At the same time, the gas temperature rapidly decreases and the VT and VV relaxation processes also contribute to the drop in the vibrational level populations and hence the vibrational temperature. On the other hand, the levels (v_7–v_{14}) are again overpopulated, with a much higher vibrational temperature of 6143 K, which can be explained by their relatively slow decay compared with the lowest vibrational levels. Indeed, the production rate of the high vibrational levels in group (v_7–v_{14}), mainly by electron impact vibrational excitation, is slightly higher than the total loss rate by VV and VT relaxation reactions at $t = 9.9 \times 10^{-3}$ s. In contrast, the total net production rate of the levels (v_1–v_6) is negative, indicating a rapid relaxation during the arc extinction stage.

The significant population of the vibrationally excited levels during the entire half cycle of the arc indicates that the

Table 7. Dominant CO_2 splitting reactions and their relative contributions, calculated for the quasi-steady state condition and transient condition, corresponding to a DC and AC gliding arc, respectively.

Process	Reaction	Relative contribution (%)	
		Quasi-steady state condition	Transient condition
1	$e^- + CO_2 v_i \rightarrow e^- + CO + O$	40	19
2	$e^- + CO_2(gr) \rightarrow e^- + CO + O$	8.4	4.1
3	$CO_2 v_i + O \rightarrow CO + O_2$	43	66
4	$CO_2(gr) + O \rightarrow CO + O_2$	5.2	8.6
5	$CO_2 v_i + O^- + M \rightarrow CO_3^- + M$	2.0	0.36
6	$CO_2(gr) + O^- + M \rightarrow CO_3^- + M$	0.46	1.3
7	$CO_2 v_i + M \rightarrow CO + O + M$	1.1	0.67
8	$CO_2(gr) + M \rightarrow CO + O + M$	6.5×10^{-4}	1.1×10^{-3}
9	$CO_2 v_i + C \rightarrow CO + CO$	8.3×10^{-4}	9.3×10^{-4}
10	$CO_2(gr) + C \rightarrow CO + CO$	1.9×10^{-4}	1.9×10^{-4}

vibrational levels will play a significant role in the CO_2 splitting. This will be illustrated in the next section.

3.2. Evaluation of the important CO_2 splitting mechanisms

3.2.1. Quasi-steady state condition. To evaluate which mechanisms are the most important for the CO_2 splitting in the gliding arc plasma, we plot in figure 8 the reaction rates of the most important CO_2 loss and formation reactions, as a function of radial position in the arc, at quasi-steady state, for the same conditions as in figure 2. The reactions are also listed in tables 7 and 8, including also their relative contributions to the overall CO_2 loss and formation. In general, it is clear that the reactions from the CO_2 vibrational levels, indicated by the dashed lines in figure 8(a), are more important than the corresponding reactions from the CO_2 ground state. The most important loss mechanism in the center of the arc appears to be electron impact dissociation from the CO_2 vibrational levels (no. 1), but its rate drops significantly as a function of radial position, because both the electron temperature (see figure 2 above) and the electron density (see figure 3 above) drop significantly for larger radial positions, so there will not be enough electrons with sufficient energy available to cause electron impact dissociation. Another loss mechanism, i.e. dissociation upon collision of O atoms with the CO_2 vibrational levels (no. 3) is also very important in the center of the arc, and its rate drops more slowly as a function of radial position, as is clear from figure 8(a), although the O atom density also drops upon increasing radial position (see figure 3 above), but as the rate of electron impact dissociation is a function of both the electron density and electron temperature, it is logical that it drops faster than the rate of dissociation upon collision with O atoms. Thus, integrated over the entire radial direction of the arc, the latter process contributes even slightly more than electron impact dissociation, with values of about 43% and 40%, respectively (see table 7). The corresponding loss processes from the CO_2 ground state (i.e. no. 2 and 4) are less important, as is clear from both figure 8 and table 7, with relative contributions of 8.4% and 5.2%, for electron impact dissociation and dissociation upon collision with O atoms, respectively. The other loss processes included in the model,

i.e. the reaction with O^- ions forming CO_3^- ions (no. 5 and 6), and dissociation upon collision with other heavy particles (i.e. no. 7–10) are of minor importance, with relative contributions of 1–2% or lower (see figure 8(a) and table 7).

The CO molecules formed upon dissociation of CO_2 will also partially recombine again in the gliding arc, yielding a lower net conversion of CO_2. The rates of the most important formation processes are somewhat lower than the rates of the most important loss processes, as depicted in figure 8(b), but they are clearly not negligible. The major formation process is the recombination of CO with O_2 (no. 1 in figure 8(b)), with a relative contribution of 60%, followed by the recombination of CO with O atoms (no. 2) and with O^- ions (no. 3), which have relative contributions of nearly 24% and 12% (see table 8), while the reaction of O atoms with CO_3^- ions (no. 4) contributes for about 4%. When comparing the total loss rate of CO_2, integrated over the entire radial direction of the arc, with the total formation rate of CO_2, we obtain values of 1.56×10^{-3} versus 1.15×10^{-3} mol·s^{-1}·m^{-1}. Thus, it is clear that about 74% of the CO_2 lost in the gliding arc, will be formed again, so the net conversion of CO_2 into CO is much smaller than the initial loss of CO_2.

3.2.2. Transient condition. As the results might be different for the AC gliding arc, because the arc ignites and extinguishes as a function of time, we plot in figure 9 the temporal evolution of the most important loss and formation rates, obtained by integrating the reaction rates over the entire arc, for the transient condition, at the same conditions as in figure 5 above. Before the arc is ignited (i.e. around $t = 10^{-4}$ s), electron impact dissociation from the CO_2 ground state (process no. 2 in figure 9(a)) is the most important loss process for CO_2, which is attributed to the relatively large electric field (see figure 5(b) above), yielding electrons with high enough energy. However, due to the low electron density at this time, the absolute rate of this process is limited. After ignition of the arc, the electric field drops dramatically, and thus, the rate of this process drops, while electron impact dissociation from the CO_2 vibrational levels (no. 1) becomes more important, as the latter process requires less energy for the electrons. When time evolves, dissociation upon collision of the CO_2

vibrational levels with O atoms (no. 3) becomes the dominant loss mechanism, as is clear from figure 9(a). Its relative contribution, integrated over time, equals 66% (see table 7), while the relative contributions of electron impact dissociation from the CO_2 vibrational levels and from the CO_2 ground state contribute for 19% and 4%, respectively. These values are different from the values calculated for the quasi-steady state condition, which is attributed to the changing conditions in the arc as a function of time. Indeed, the average discharge current over one half cycle is around 15.9 mA, which is higher than the value in the quasi-steady state case (i.e. 10 mA), and hence the average electric field in the transient condition is lower, yielding a lower relative contribution of electron impact dissociation.

The relative importance of the main formation mechanisms of CO_2, however, is not so much different from the results under the quasi-steady state condition (see table 8), although recombination of CO with O_2 becomes more important, and recombination with O^- ions becomes less important. When again comparing the total rate of all CO_2 loss processes integrated over time (i.e. 2.45×10^{-5} mol $\cdot$ m^{-1}), with the total rate of all formation mechanisms (i.e. 1.79×10^{-5} mol $\cdot$ m^{-1}), it is clear that about 73% of the CO_2 lost in the gliding arc, will be formed again, which is very similar to the quasi-state state condition.

It is noted that previous theoretical and experimental investigations from literature also indicated that stimulation of vibrational excitation of CO_2 molecules is the most effective route for CO_2 dissociation in a microwave plasma [22, 66]. Our calculated results here also reveal that non-equilibrium vibrational excitation of CO_2 promotes efficient dissociation in the gliding arc, and this is consistent with experimental investigation in literature. Indeed, the experimental work for both a gliding arc plasmatron [9] and diverging electrodes gliding arc reactors [10] shows that the presence of a very small quantity of water during CO_2 dissociation greatly reduces the power efficiency compared with pure CO_2. This is explained by the fact that water can significantly reduce the vibrational excitation of CO_2 molecules, because the energy is absorbed and quickly lost by water. Based on this, Nunnally *et al* [9] concluded that non-equilibrium vibrational excitation plays the major role during CO_2 dissociation in a gliding arc. Therefore, these experimental results support our modelling results.

3.3. Effect of the characteristic frequency of convective cooling on the plasma characteristics and the CO_2 conversion processes

As mentioned in the model description (section 2.1 above), we apply a characteristic frequency of convective cooling, to account for losses in the plasma species and in the heat upon convection due to the gas flow. In previous section, we assumed a value for this characteristic frequency of 2.5 kHz, but as the actual value is not known, we want to evaluate the effect of this assumption on the calculation results. Figure 10 shows the radial distribution of the gas temperature, the electron number density, the electron temperature and the vibrational temperature for the transient condition, at $t = 10^{-3}$ s, for different characteristic frequencies of convective cooling.

Table 8. Dominant CO_2 formation reactions and their relative contributions, calculated for the quasi-steady state condition and transient condition, corresponding to a DC and AC gliding arc, respectively.

		Relative contribution	
Process	Reaction	Quasi-steady state condition	Transient condition
1^a	$CO + O_2 \rightarrow CO_2 + O$	60	75
2	$CO + O + M \rightarrow CO_2 + M$	24	23
3	$CO + O^- \rightarrow e^- + CO_2$	12	1.6
4	$O + CO_3^- \rightarrow CO_2 + O_2^-$	4.4	0.67

^{a} O_2 represents the ground state and the vibrational states of molecular oxygen.
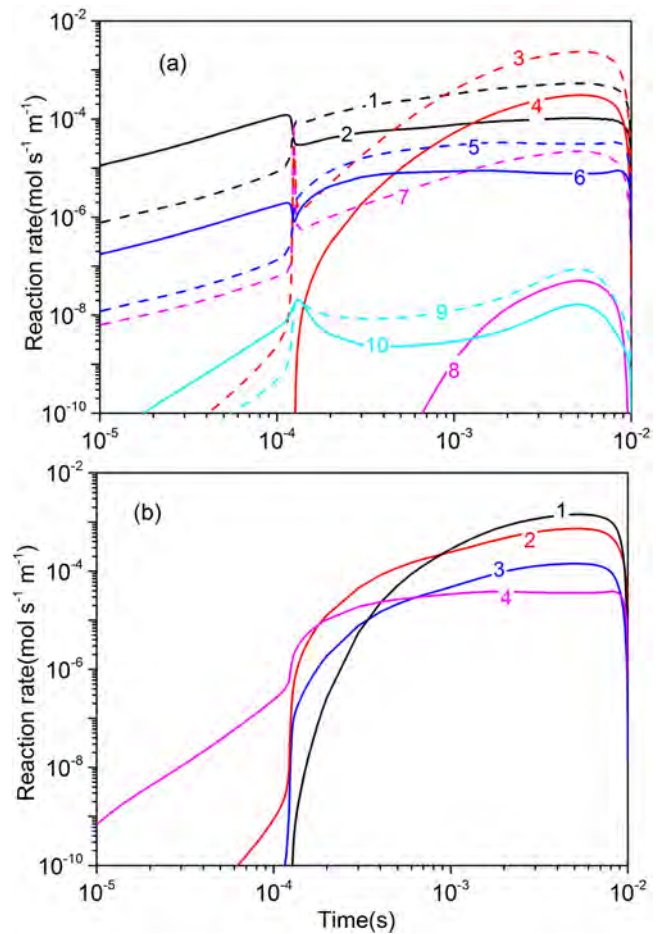
Figure 9. Time evolution of the spatially-integrated rates over the entire arc, for CO_2 loss (a) and formation (b) by the most important processes, at the same conditions as in figure 5. The numbers of the curves correspond to the reactions listed in tables 7 and 8 for the CO_2 loss and formation mechanisms, respectively. The reactions from the CO_2 vibrational levels are indicated with dashed lines in (a), while the reactions with the CO_2 ground state are plotted with solid lines.

We can anticipate that a larger characteristic frequency of convective cooling results in more power dissipation by the cooling effect of the convective flow, thus yielding a somewhat lower gas temperature as a function of radial position, as indicated in figure 10(a). This corresponds to a contraction of the discharge channel, which is also reflected from the electron
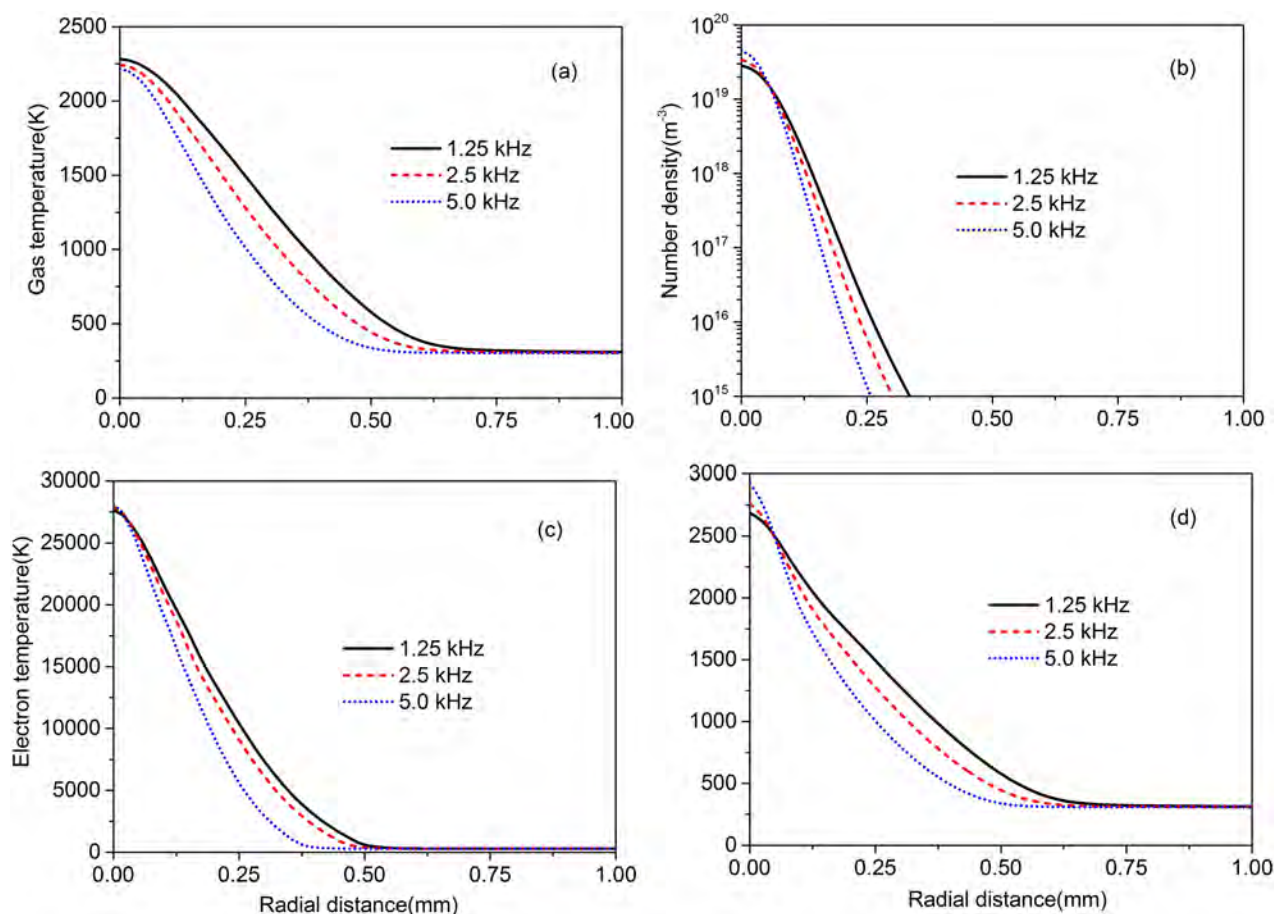
Figure 10. Radial distribution of the gas temperature (a), electron number density (b), electron temperature (c), and vibrational temperature of the asymmetric mode $T_{vI}(CO_2)$ (d) for the transient condition, at $t = 10^{-3}$ s and different frequencies of convective cooling.

number density distribution, showing a narrower arc and higher values at the arc center at higher frequency of convective cooling (see figure 10(b); note the logarithmic scale). The electron temperature is also slightly higher in the arc center and drops faster as a function of radial position with rising value of the characteristic frequency of convective cooling, caused by the higher Joule heating effect in a contracted channel (figure 10(c)). The higher electron temperature and electron number density in the arc center give somewhat more vibrational excitation, and thus, the vibrational temperature becomes also slightly higher in the center (figure 10(d)), indicating that a larger overpopulation of the vibrational states can be reached. The deviation of the various temperatures caused by different characteristic frequencies of convective cooling becomes somewhat larger beyond the arc center, indicating that the influence of convective cooling is becoming larger when the electric heating effect is decreasing. In general, it is clear that a higher frequency of convective cooling results in a somewhat more contracted arc, because the temperatures drop faster as a function of radial position, but the absolute values of the different temperatures at the arc center do not change a lot when varying this frequency from 1.25 to 5 kHz.

The characteristic frequency of convective cooling has quite some influence on the relative contributions of the various processes for CO_2 loss and formation, as presented in figure 11. Indeed, electron impact dissociation from the CO_2 vibrational levels (reaction no. 1) becomes gradually more important, while dissociation upon collision of the CO_2 vibrational levels with O atoms (no. 3) becomes less important upon rising value of the characteristic frequency of convective cooling. This can be explained because the convective cooling results in some contraction of the arc, as illustrated above, yielding a somewhat higher electron number density and temperature in the center of the arc, which causes more electron impact dissociation of CO_2. In contrast, dissociation upon collision of CO_2 with O atoms becomes somewhat less important when there is more convective cooling, due to the lower gas temperature. However, the relative order of importance of both processes remains the same for the different values of the characteristic frequency. The same (increasing and decreasing) trend is also observed for the relative contributions of electron impact dissociation and dissociation upon collision of O atoms with the CO_2 ground state (reactions 2 and 4, respectively), but their contributions are much lower. The contributions of the other loss processes for CO_2 (i.e. reactions no. 5–10 in table 7) are virtually negligible, whatever the assumption of the characteristic frequency of convective cooling.

As far as the formation processes are concerned, recombination of CO with O_2 (i.e. reaction no. 1 in table 8) becomes gradually less important, while the other processes become gradually more important upon rising value of the characteristic frequency of convective cooling, with the recombination

of CO with O atoms (i.e. reaction no. 2 in table 8) becoming of comparable importance at 5 kHz.

The total rates of CO_2 loss and formation both decrease to some extent upon rising value of the characteristic frequency of convective cooling. However, the drop in total CO_2 loss rate is smaller than the drop in total CO_2 formation rate (i.e. 52% versus 71% from 1.25 kHz to 5 kHz). Therefore, the net conversion rate of CO_2 will rise when assuming a higher characteristic frequency of convective cooling, as is clearly indicated in figure 12. When integrating over one half discharge cycle, the total (net) CO_2 conversion per gliding arc length ζ amounts to 3.5×10^{-6} mol · m^{-1}, 6.6×10^{-6} mol · m^{-1} and 8.5×10^{-6} mol · m^{-1}, for the characteristic frequencies of convective cooling equal to 1.25, 2.5 and 5 kHz. As mentioned above, our model does not allow the calculation of the overall CO_2 conversion, as the latter requires a detailed description of the flow rate and the reactor geometry, which is not possible in our 1D model. However, from the consumed energy in the plasma and the total net CO_2 conversion mentioned above within a processing time $\Delta t = 10$ ms, for a gliding arc with a length l, we can obtain the so-called power efficiency, which is a measure of the system efficiency and calculated as [10]:

$$\eta = \frac{\text{total converted } CO_2}{\text{total consumed energy}} = \frac{\zeta l N_A}{P_0 l \Delta t} = \frac{\zeta N_A}{P_0 \Delta t} \quad (32)$$

where N_A is Avogadro's constant and P_0 is the discharge power per unit length, which is calculated from the electric field (E) and electric current (I) in the model, as follows: $P_0 = \frac{\int_0^{\Delta t} EI \, dt}{\Delta t}$.

For the assumed characteristic frequencies of convective cooling equal to 1.25, 2.5 and 5 kHz, P_0 is calculated to be 2048 W · m^{-1}, 2260 W · m^{-1} and 2439 W · m^{-1}, respectively, and the corresponding power efficiencies, obtained from these power values and the total net conversion mentioned above, amount to 1.03×10^{17} J^{-1}, 1.76×10^{17} J^{-1} and 2.10×10^{17} J^{-1}. Because a higher characteristic frequency of convective cooling typically corresponds to a higher gas flow velocity, this increasing trend of the power efficiency means that more CO_2 molecules can be converted at higher gas flow rates than at lower flow rates, because of the higher total number of CO_2 molecules passing through the arc. Without considering the exact flow rate and the reactor geometry in our 1D model, it is not possible to give an accurate comparison with experimental investigations. However, this increasing trend is qualitatively in agreement with experimental results [10], where power efficiencies for CO_2 conversion ranging from 2.5×10^{17} J^{-1} to 3.7×10^{17} J^{-1} were reported for gas flow rates varying from 0.8 l min^{-1} to 1.5 l min^{-1}.

This trend of increasing net conversion rate, upon increasing value of the assumed frequency of convective cooling can be explained from figure 10. Indeed, a higher frequency of convective cooling yields a slightly higher electron number density and electron temperature in the arc center, which favour electron impact dissociation of CO_2. Additionally, a somewhat higher vibrational temperature is reached, indicating a somewhat higher population of the vibrational states, which also contribute to more CO_2 conversion, due to electron impact dissociation. However, in spite of the higher vibrational temperature and hence a larger overpopulation of the vibrational
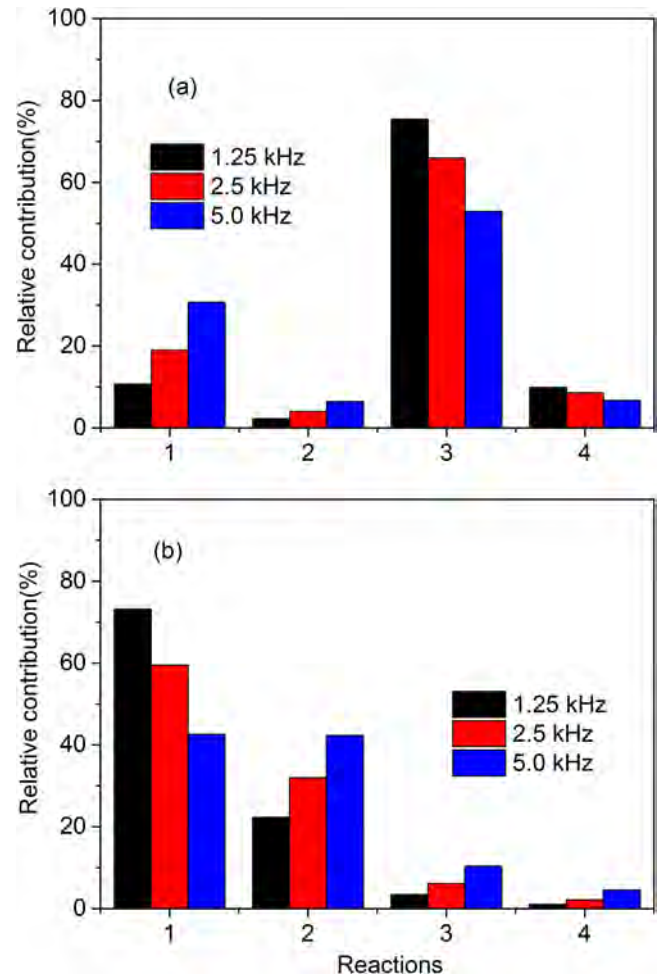

Figure 11. Relative contribution of the most important processes for CO_2 loss (a) and formation (b), at different characteristic frequencies of convective cooling for the transient condition at $t = 10^{-3}$ s. The reaction numbers in the *x*-axis of (a) and (b) correspond to the numbers in tables 7 and 8, respectively. Note that only the four main loss processes are illustrated in (a).

levels, the dissociation rate due to collisions with O atoms decreases as a result of the somewhat lower gas temperature, as also mentioned above. Nevertheless, because the reaction rates of the dominant CO_2 formation reactions (reactions no. 1 and 2 in table 8) also strongly depend on the gas temperature, the formation of CO_2 drops significantly upon rising characteristic frequencies of convective cooling, and thus, the total net CO_2 conversion rate increases.

3.4. Validity of the lumped-level strategy

We have illustrated above that the present 1D model can describe some basic characteristics of the gliding arc, but it cannot account for all geometrical effects, and therefore it cannot yet predict the overall CO_2 conversion in the gliding arc. For this purpose, a 2D or even 3D model would be needed. However, such a model is computationally much more demanding, and will require a reduction of the chemistry set. As a large fraction of the chemistry is related to the CO_2 vibrational levels, more specifically to those of the asymmetric mode, a reduction of the number of vibrational levels
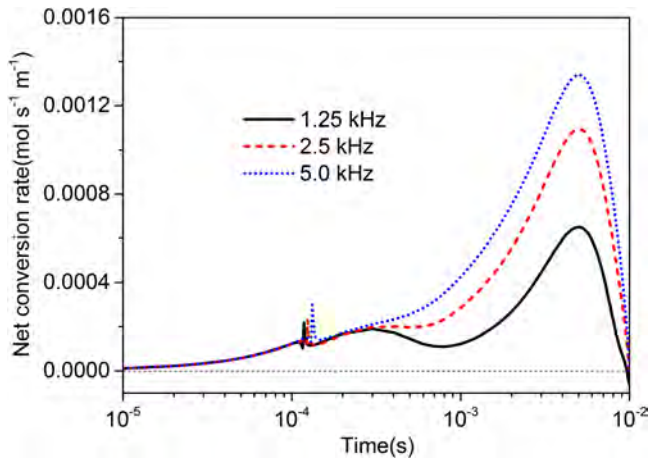
Figure 12. Time evolution of the spatially integrated net conversion rate of CO_2 for different frequencies of convective cooling, at the same condition as in figure 10.

would be beneficial for speeding up the calculations. However, because vibrational excitation plays an important role in the CO_2 dissociation, as shown in figures 8 and 9 above, an accurate description of the VDF is needed. In previous work from our group [31] the effectiveness of a lumped-level approach was investigated for a microwave plasma by a 0D model. In the present work, we check the validity of this lumped-level strategy for the gliding arc in this 1D model, so that we can use this strategy in the next step of our investigations, for modelling the CO_2 conversion in a real gliding arc.

In figure 13 the normalized VDFs, obtained by the full model, the 3 different lumped-levels models with 1, 2 or 3 groups, as well as the thermal distribution model, are presented for three different moments in time, corresponding to the arc initiation, the peak current and the arc extinction stage. It is clear that the lumped-levels model with 3 groups can reproduce the VDF obtained with the full model quite well. Only at the time of arc ignition, there is some deviation of the higher vibrational levels, but at the later times, the agreement is excellent. The lumped-levels models with 2 groups and 1 group can only reproduce the VDF at the time of the peak current, where the VDF nearly follows a Maxwellian distribution, but at the time of arc ignition or extinction, a clear deviation is seen for the 2-groups model, and even more for the 1-group model. Finally, the thermal distribution model, which assumes a Maxwellian distribution for the asymmetric mode, based on the gas temperature, does not at all coincide with the VDF calculated with the full model. Thus, it is clear that only the 3-groups can reasonably reproduce the actual VDF, over the entire time-period from arc ignition to arc extinction in one half cycle of the AC gliding arc.

Nevertheless, when comparing the time evolution of the gas temperature, electron temperature and electron number density at the arc center, as well as the spatially-integrated molar fraction of CO over the whole discharge channel, as calculated by the different models (see figure 14), it is clear that besides the 3-groups lumped-levels model, also the 2-groups and 1-group model yield a good agreement with the results predicted by the full model, in spite of the fact that
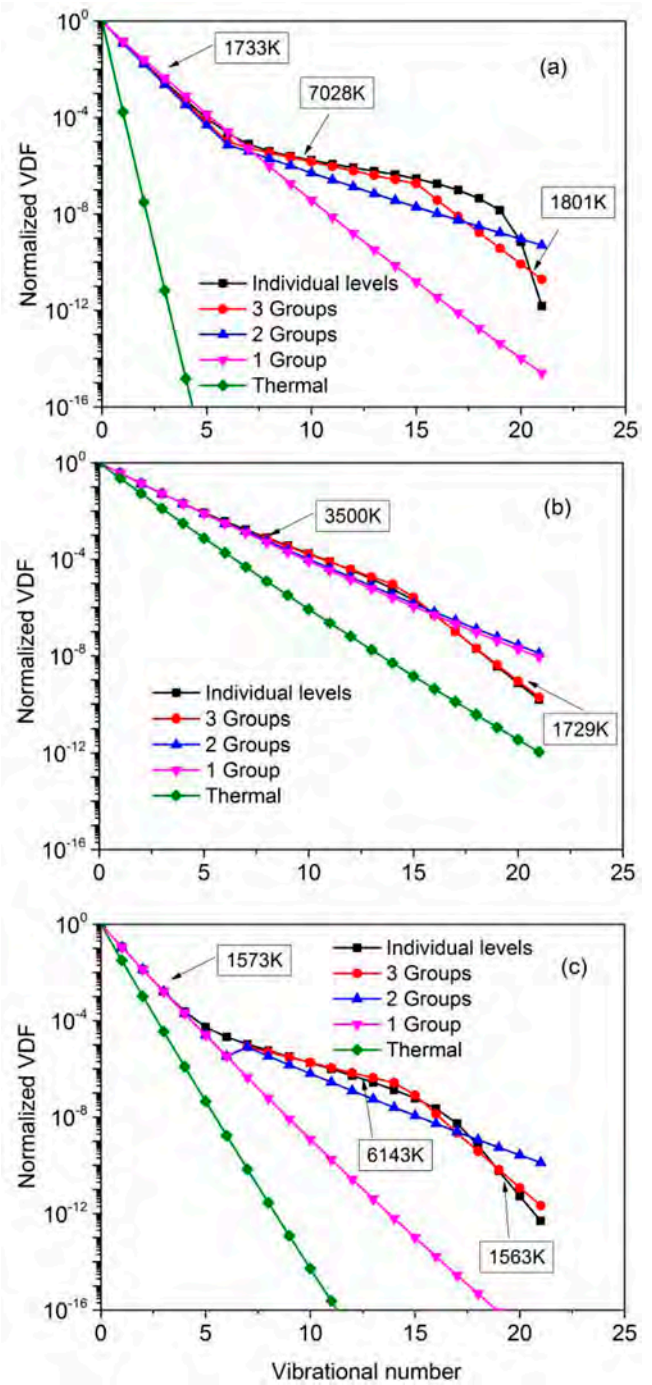
Figure 13. VDFs at $t = 1.2 \times 10^{-4}$ s (a), 5×10^{-3} s (b) and 9.9×10^{-3} s (c), which correspond to the time of gliding arc discharge initiation, the time of the peak current and of the arc extinction stage, respectively (see figure 5(a) above). Comparison is made between the VDFs predicted by the full model, the different lumped-levels models and the thermal distribution model.

the VDFs calculated by these models showed a clear deviation. This indicates that the dissociation from the lowest vibrational levels is more important at these conditions, and the latter explains why the different lumped-levels models give good agreement with the full model, as they all represent well the VDF for the lowest vibrational levels. On the other hand, the model assuming a thermal distribution for the asymmetric mode vibrational levels based on the gas temperature predicts
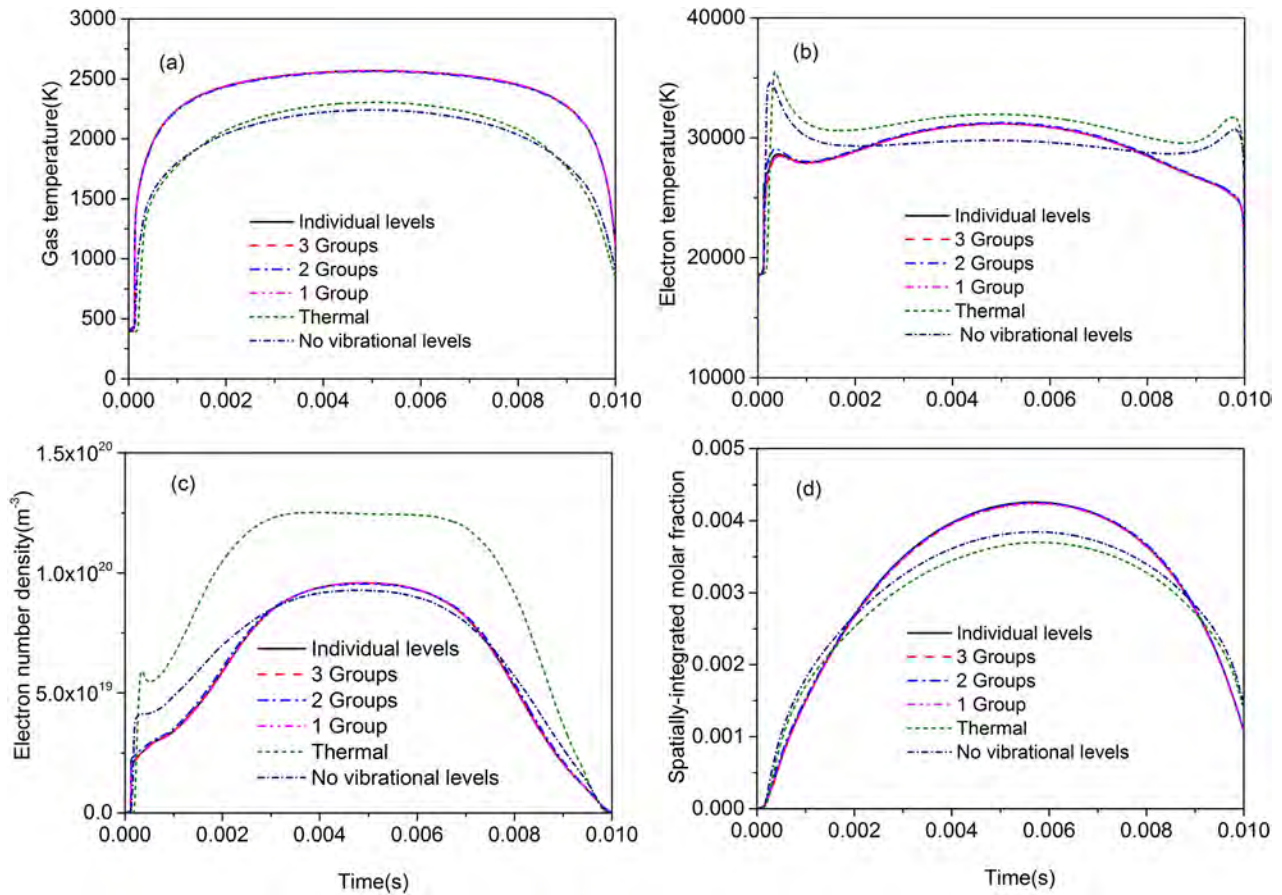
Figure 14. Time evolution of the gas temperature (a), electron temperature (b), electron number density (c) at the center of the arc and the spatially-integrated molar fraction of CO over the whole discharge channel (d), calculated with the different models (see legend).

a lower gas temperature, a higher electron temperature and a higher electron number density. This is because the thermal distribution model does not guarantee the conservation of energy, which results here in a loss of vibrational energy and it underestimates the VT relaxation processes and hence the gas temperature, and this leads to a somewhat contracted discharge channel. As a result, the electron temperature and electron number density are somewhat overestimated at the center, in order to keep the same discharge current. Additionally, the thermal distribution model underestimates the spatially-integrated molar fraction of CO between 2×10^{-3} s and 9×10^{-3} s, when the discharge current is high, because the dissociation rate upon collision of CO_2 (either the ground state or the vibrational levels, reaction no. 3 and 4 in table 7) with O atoms is greatly underestimated as a result of the lower gas temperature. On the other hand, this model overestimates the spatially-integrated molar fraction of CO when the arc is ignited ($t < 2 \times 10^{-3}$ s) and extinguished ($t > 9 \times 10^{-3}$ s). This is because the electron impact dissociation rate (reaction no. 1 and 2 in table 7, see figure 9) is overestimated due to the higher electron temperature and electron number density at these times. The same reason can also explain the effect of ignoring the vibrational levels of the asymmetric mode of CO_2 on the spatially-integrated molar fraction of CO This model also underestimates the population of the vibrational levels and hence the heating source term of the gas translational temperature by VT relaxation, yielding a lower gas temperature. At

the same time, the electron energy loss due to vibrational excitation to the asymmetric states of CO_2 is ignored, and thus it overestimates the electron temperature, thus yielding more electron impact ionization and a larger electron density upon arc ignition ($t < 2.5 \times 10^{-3}$ s) and extinction ($t > 7.5 \times 10^{-3}$ s). Upon further increase of the discharge current, for example, from 2.5×10^{-3} s to 7.5×10^{-3} s, the discharge channel gradually becomes broader than what is estimated by the full model, due to the neglected electron energy loss in the outer plasma region. Therefore, the model ignoring the vibrational levels of the asymmetric mode of CO_2 slightly underestimates the electron temperature and electron number density in the arc centre but overestimates both of them in the plasma edge.

Thus we can conclude that neglecting the vibrational kinetics or assuming a thermal vibrational distribution for the asymmetric mode are too rough approximations for an accurate description of the gliding arc behaviour, but the lumped-level approach, even with only 1 group, yields a reasonable prediction of the main plasma characteristics, including information on the CO_2 conversion. However, for an accurate description of the VDF, a 3-groups model is the most appropriate, as was also observed for the MW plasma [31].

4. Conclusion

In this paper we describe a 1D quasi-gliding arc model in a cylindrical frame, with detailed non-equilibrium CO_2 plasma

chemistry, including the CO_2 vibrational kinetics, in order to obtain a better understanding of the basic plasma characteristics and underlying mechanisms of CO_2 conversion in a gliding arc plasma. The equations solved in the model and the plasma chemistry taken into account are explained in detail. Although the model is only 1D and can thus not describe the geometrical effects and the detailed effect of the gas flow on the arc dynamics, it does account for the loss of plasma species and heat due to convection by the gas flow, by means of a characteristic frequency for convective cooling.

The model calculates the VDF of the asymmetric mode of CO_2, from which the vibrational temperature(s) can be deduced. Also the radial distribution of the gas temperature, the electron temperature and the molar fractions of the various neutral and charged species are calculated, both under quasi-steady state and transient conditions, corresponding to a DC and AC gliding arc, respectively. It is clear that a large fraction of the CO_2 molecules is split into CO, O and O_2, but only in the center of the arc, which is characterized by the highest gas temperature, electron temperature and vibrational temperature. At less than 0.5 mm from the center, the CO_2 splitting is already negligible. The ionization degree is at maximum 10^{-5} in the center of the arc, and also drops dramatically as a function of radial position. For the AC gliding arc, we also calculated the temporal behavior of the various temperatures, the electric field and molar fractions of the neutral and charged species, during arc ignition, stable arc evolution and arc extinction.

In this work, a detailed validation of our model by direct comparison under the specific conditions has not been included due to the lack of concrete experimental plasma parameters of a pure CO_2 gliding arc in the literature. To our knowledge, the only experimental data available for a CO_2 gliding arc are presented in [65], but this was for a 'tornado' discharge using CO_2 doped with 1% N_2. Hence, it is not possible to exactly compare the data, as they are obtained in a different gliding arc setup with different reactor geometry and discharge conditions. Nevertheless, the agreement between our calculations results and the experimental data for the gas temperature and vibrational temperature is quite reasonable, keeping in mind also the limitations of the 1D model. In addition, our calculation shows that typical non-equilibrium characteristics, i.e. a much higher electron temperature and vibrational temperature than the gas temperature, prevails in the gliding arc and this is also qualitatively in agreement with the experimental observation of gliding arc.

We have also investigated the relative contributions of the various processes responsible for the loss (and production) of CO_2 in the gliding arc. It is clear that the vibrational levels play the most important role in the CO_2 conversion. The experimental investigations of CO_2 gliding arc in literature also support this prediction. Therefore, we may conclude that our model already gives a good qualitative insight in the underlying processes of gliding arc based CO_2 conversion. Dissociation upon collision with O atoms, and to a lower extent also electron impact dissociation of these vibrational levels are the major loss mechanisms. However, a fraction of

the CO formed will also be converted back into CO_2, mainly upon recombination with O_2 molecules, as well as O atoms or O^- ions.

To evaluate the effect of the characteristic frequency of convective cooling on the calculation results, we have varied this parameter within a range, corresponding to typical experimental conditions. A higher value of this characteristic frequency leads to some contraction of the arc, yielding a somewhat higher electron density, electron temperature and vibrational temperature in the center, which drop faster as a function of radial position. It also yields a slightly lower gas temperature, and it affects the relative contributions of the CO_2 loss and formation processes to some extent, but the general calculation results and conclusions remain unaltered.

As the 1D model does not account for the real gas flow effects, it does not yet allow to predict the overall CO_2 conversion in the gliding arc. However, from the calculated CO_2 conversion rate and the total consumed energy, information could be obtained about the system power efficiency for conversion, and these values are found to be in reasonable agreement with the experimental data from literature.

Finally, the effect of lumping the vibrational levels of the asymmetric mode of CO_2 into 1, 2 or 3 groups is assessed, by comparing the calculated VDFs, gas temperature, electron temperature and electron number density, as well as the obtained CO molar fraction, with the results of the full model, describing all levels separately. It seems that the lumping strategy, with either 1, 2 or 3 groups, is able to reproduce the plasma characteristics very well, but only the 3-groups model is able to describe the typical shape of the VDF in a gliding arc plasma. A model assuming a thermal vibrational distribution based on the gas temperature or a model neglecting the vibrational kinetics of the asymmetric mode, however, yield significant deviations in the calculated plasma characteristics.

In reality, the gliding arc problem is a 3D problem and we can only compare the results from a 3D model quantitatively with experiments. However, the 3D model of CO_2 gliding arc with considering the full reaction set with a large number of 40 species causes the computational load to become prohibitive. Therefore, the fact that the lumping strategy generally yields good agreement with the full model, with a significant reduction in the calculation time, opens perspectives for modeling CO_2 conversion in the gliding arc by means of 2D or 3D models. This will be the subject of our future work.

Acknowledgments

References

[1] Czernichowski A 1994 Gliding arc. Applications to engineering and environment control *Pure Appl. Chem.* **66** 1301–10

[2] Fridman A, Nester S, Kennedy L A, Saveliev A and Mutaf-Yardimci O 1999 Gliding arc gas discharge *Prog. Energy Combust. Sci.* **25** 211–31

[3] Richard F, Cormier J M, Pellerin S and Chapelle J 1997 Gliding arcs fluctuations and arc root displacement *High Temp. Mater. Process.* **1** 239–48

[4] Du C M *et al* 2014 Plasma reforming of bio-ethanol for hydrogen rich gas production *Appl. Energy* **133** 70–9

[5] Kalra C S, Gutsol A F and Fridman A A 2005 Gliding arc discharges as a source of intermediate plasma for methane partial oxidation *IEEE Trans. Plasma Sci.* **33** 32–41

[6] Sreethawong T, Thakonpatthanakun P and Chavadej S 2007 Partial oxidation of methane with air for synthesis gas production in a multistage gliding arc discharge system *Int. J. Hydrog. Energy* **32** 1067–79

[7] Tu X and Whitehead J C 2014 Plasma dry reforming of methane in an atmospheric pressure AC gliding arc discharge: cogeneration of syngas and carbon nanomaterials *Int. J. Hydrog. Energy* **39** 9658–69

[8] Chun Y N and Song H O 2008 Syngas production using gliding arc plasma *Energy Sources A: Recovery Util. Environ. Eff.* **30** 1202–12

[9] Nunnally T, Gutsol K, Rabinovich A, Fridman A, Starikovsky A and Gutsol A 2011 Dissociation of CO_2 in a low current gliding arc plasmatron *J. Phys. D: Appl. Phys.* **44** 274009

[10] Indarto A, Yang D R, Choi J W, Lee H and Song H K 2007 Gliding arc plasma processing of CO_2 conversion *J. Hazard. Mater.* **146** 309–15

[11] Kim S C, Lim M S and Chum Y N 2014 Reduction characteristics of carbon dioxide using a plasmatron *Plasma Chem. Plasma Process.* **34** 125–43

[12] Pellerin S, Cormier J M, Richard F, Musiol K and Chapelle J 1999 Determination of electrical parameters of bi-dimensional DC Glidarc *J. Phys. D: Appl. Phys.* **32** 891–7

[13] Czernichowski A, Nassar H and Ranaivosoloarimanana A 1996 Spectral and electrical diagnostics of gliding arc *Acta Phys. Pol.* A **89** 595–603

[14] Mutaf-Yardimci O, Saveliev A V, Fridman A A and Kennedy L A 2000 Thermal and nonthermal regimes of gliding arc discharge in air flow *J. Appl. Phys.* **87** 1632–41

[15] Tu X, Gallon H.J and Whitehead J C 2011 Dynamic behavior of an atmospheric argon gliding arc plasma *IEEE Trans. Plasma Sci.* **39** 2900–1

[16] Richard F, Cormier J M, Pellerin S and Chapelle J 1996 Physical study of a gliding arc discharge *J. Appl. Phys.* **79** 2245–50

[17] Pellerin S, Richard F, Chapelle J, Cormier J M and Musiol K 2000 Heat string model of bi-dimensional DC Glidarc *J. Phys. D: Appl. Phys.* **33** 2407–19

[18] Kuznetsova I V, Kalashnikov N Y, Gutsol A F, Fridman A A and Kennedy L A 2002 Effect of 'overshooting' in the transitional regimes of the low-current gliding arc discharge *J. Appl. Phys.* **92** 4231–7

[19] Kolev St and Bogaerts A 2015 A 2D model for a gliding arc discharge *Plasma Sources Sci. Technol.* **24** 015025

[20] Kolev St and Bogaerts A 2015 Similarities and differences between gliding glow and gliding arc discharges *Plasma Sources Sci. Technol.* **24** 065023

[21] Trenchev G, Kolev St and Bogaerts A 2015 A 3D model of a reverse vortex flow gliding arc reactor *Plasma Sources Sci. Technol.* **25** 035014

[22] Fridman A 2008 *Plasma Chemistry* (Cambridge: Cambridge University Press)

[23] Gutsol A, Rabinovich A and Fridman A 2011 Combustion-assisted plasma in fuel conversion *J. Phys. D: Appl. Phys.* **44** 274001

[24] Kozák T and Bogaerts A 2014 Splitting of CO_2 by vibrational excitation in non-equilibrium plasmas: a reaction kinetics model *Plasma Sources Sci. Technol.* **23** 045004

[25] Kozák T and Bogaerts A 2015 Evaluation of the energy efficiency of CO_2 conversion in microwave discharges using a reaction kinetics model *Plasma Sources Sci. Technol.* **24** 015024

[26] Snoeckx R, Aerts R, Tu X and Bogaerts A 2013 Plasma-based dry reforming: a computational study ranging from the nanoseconds to seconds time scale *J. Phys. Chem.* C **117** 4957–70

[27] Heijkers S, Snoeckx R, Kozák T, Silva T, Godfroid T, Britun N, Snyders R and Bogaerts A 2015 CO_2 conversion in a microwave plasma reactor in the presence of N_2: elucidating the role of vibrational levels *J. Phys. Chem.* C **119** 12815–28

[28] Pietanza L D, Colonna G, D'Ammando G, Laricchiuta A and Capitelli M 2015 Vibrational excitation and dissociation mechanisms of CO_2 under non-equilibrium discharge and post-discharge conditions *Plasma Sources Sci. Technol.* **24** 042002

[29] Aerts R, Martens T and Bogaerts A 2012 Influence of vibrational states on CO_2 splitting by dielectric barrier discharges *J. Phys. Chem.* C **116** 23257–73

[30] Aerts R, Somers W and Bogaerts A 2015 Carbon dioxide splitting in a dielectric barrier discharge plasma: a combined experimental and computational study *ChemSusChem* **8** 702–16

[31] Berthelot A and Bogaerts A 2016 Modeling of plasma-based CO_2 conversion: lumping of the vibrational levels *Plasma Sources Sci. Technol.* **25** 045022

[32] Shneider M N, Mokrov M S and Milikh G M 2014 Dynamic contraction of the positive column of a self-sustained glow discharge in air flow *Phys. Plasmas* **21** 032122

[33] Shneider M N, Mokrov M S and Milikh G M 2012 Dynamic contraction of the positive column of a self sustained glow discharge in molecular gas *Phys. Plasmas* **19** 033512

[34] Kolev St, Sun S R, Trenchev G, Wang W Z, Wang H X and Bogaerts A 2016 Modeling of gliding arc plasmas *Plasma Process Polym.* at press

[35] Hagelaar G J M and Pitchford L C 2005 Solving the Boltzmann equation to obtain electron transport coefficients and rate coefficients for fluid models *Plasma Sources Sci. Technol.* **14** 722–33

[36] Viehland L A and Mason E A 1995 Transport properties of gaseous ions over a wide energy range, IV *At. Data Nucl. Data Tables* **60** 37–95

[37] Ellis H W, Pai R Y, McDaniel E W, Mason E A and Viehland L A 1976 Transport properties of gaseous ions over a wide energy range *At. Data Nucl. Data Tables* **17** 177–210

[38] Ponduri S, Becker M M, Welzel S, van de Sanden M C M, Loffhagen D and Engeln R 2016 Fluid modelling of CO_2 dissociation in a dielectric barrier discharge *J. Appl. Phys.* **119** 093301

[39] McDaniel E W and Mason E A 1973 *The Mobility and Diffusion of Ions in Gases* (Hoboken, NJ: Wiley)

[40] Wang W Z, Rong M Z, Wu Y and Yan J D 2014 Fundamental properties of high-temperature SF_6 mixed with CO_2 as a replacement for SF_6 in high-voltage circuit breakers *J. Phys. D: Appl. Phys.* **47** 255201

[41] www.comsol.com

[42] Bogaerts A, Wang W Z, Berthelot A and Guerra V 2016 Modeling plasma-based CO_2 conversion: crucial role of the

dissociation cross section *Plasma Sources Sci. Technol.* **25** 055016

[43] Lowke J J, Phelps A V and Irwin B W 1973 Predicted electron transport coefficients and operating characteristics of CO_2–N_2–He laser mixtures *J. Appl. Phys.* **44** 4664–71

[44] Suzuki I 1968 General anharmonic force constants of carbon dioxide *J. Mol. Spectrosc.* **25** 479–500

[45] Phelps Database 2016 www.lxcat.net (Accessed: 17 January 2016)

Lawton S A and Phelps A V 1978 Excitation of the $b1\Sigma_g^+$ state of O_2 by low energy electrons *J. Chem. Phys.* **69** 1055–68

[46] Land J E 1978 Electron scattering cross sections for momentum transfer and inelastic excitation in carbon monoxide *J. Appl. Phys.* **49** 5716–21

[47] Cenian A, Chernukho A, Borodin V and Sliwinski G 1994 Modeling of plasma-chemical reactions in gas mixture of CO_2 lasers I. Gas decomposition in pure CO_2 glow discharge *Contrib. Plasma Phys.* **34** 25–37

[48] Hokazono H and Fujimoto H 1987 Theoretical analysis of the CO_2 molecule decomposition and contaminants yield in transversely excited atmospheric CO_2 laser discharge *J. Appl. Phys.* **62** 1585–94

[49] Beuthe T G and Chang J S 1997 Chemical kinetic modelling of non-equilibrium Ar–CO_2 thermal plasmas *Japan. J. Appl. Phys.* **36** 4997–5002

[50] Eliasson B, Hirth M and Kogelschatz U 1987 Ozone synthesis from oxygen in dielectric barrier discharges *J. Phys. D: Appl. Phys.* **20** 1421–37

[51] Cenian A, Chernukho A and Borodin V 1995 Modeling of plasma-chemical reactions in gas mixture of CO_2 lasers. II. Theoretical model and its verification *Contrib. Plasma Phys.* **35** 273–96

[52] Gudmundsson J T and Thorsteinsson E G 2007 Oxygen discharges diluted with argon: dissociation processes *Plasma Sources Sci. Technol.* **16** 399–412

[53] Woodall J, Agúndez M, Markwick-Kemper A J and Millar T J 2007 The UMIST database for astrochemistry 2006 *Astron. Astrophys.* **466** 1197–204

[54] Blauer J A and Gilmore G R 1973 A survey of vibrational relaxation rate data for processes important to CO_2–N_2–H_2O infrared plume radiation *Technical Report* AFRPL-TR-73-57, Ultrasystems, Inc.

[55] Sharma R D 1969 Near resonant vibrational energy transfer among isotopes of CO_2 *Phys. Rev.* **177** 102–7

[56] Kreutz T G, O'Neill J A and Flynn G W 1987 Diode laser absorption probe of vibration energy transfer in CO_2 *J. Phys. Chem.* **91** 5540–3

[57] Mick H-j, Burmeister M and Roth P 1993 Atomic resonance absorption spectroscopy measurements on high-temperature CO dissociation kinetics *AIAA J.* **31** 671–6

[58] Hadj-Ziane S, Held B, Pignolet P, Peyrous R and Coste C 1992 Ozone generation in an oxygen-fed wire-to-cylinder ozonizer at atmospheric pressure *J. Phys. D: Appl. Phys.* **25** 677–85

[59] Wang Y, Li X D, Yu L and Yan J H 2011 Numerical simulation study on characteristics of gliding arc discharge *Acta Phys. Sin.* **60** 035203

[60] Gangoli S P, Gutsol A F and Fridman A A 2010 A non-equilibrium plasma source: magnetically stabilized gliding arc discharge: I. Design and diagnostics *Plasma Sources Sci. Technol.* **19** 065003

[61] Gangoli S P 2007 Design and preliminary characterization of the magnetically stabilized gliding arc *Master Thesis* Drexel University

[62] Zhu J, Gao J, Ehn A, Li Z, Aldén M, Salewski M and Kusano Y 2014 Translational, rotational and vibrational temperatures of a gliding arc discharge at atmospheric pressure air *14th Int. Symp. on High Pressure Low Temperature Plasma Chemistry: Book of Contributions (INP Greifswald)* ed R Brandenburg and L Stollenwerk

[63] Wu A J, Yan J H, Zhang H, Zhang M, Du C M and Li X D 2014 Study of the dry methane reforming process using a rotating gliding arc reactor *Int. J. Hydrog. Energy* **39** 17656–70

[64] Zhao T L, Xu Y, Song Y H, Li X S, Liu J L, Liu J B and Zhu A M 2013 Determination of vibrational and rotational temperatures in a gliding arc discharge by using overlapped molecular emission spectra *J. Phys. D: Appl. Phys.* **46** 345201

[65] Nunnally T 2011 Application of low current gliding arc plasma discharges for hydrogen sulfide decomposition and carbon dioxide emission reduction *PhD Thesis* Drexel University

[66] Rusanov V D, Fridman A A and Sholin G V 1981 The physics of a chemically active plasma with nonequilibrium vibrational excitation of molecules *Sov. Phys. Usp.* **24** 447